J. Fluid Mech. (2017), *vol.* 817, *pp.* 80–121. © Cambridge University Press 2017
doi:10.1017/jfm.2017.88

Nonlinear unsteady streaks engendered by the interaction of free-stream vorticity with a compressible boundary layer

Elena Marensi[1,2,†], Pierre Ricco[1] and Xuesong Wu[3]

[1]Department of Mechanical Engineering, The University of Sheffield, S1 3JD Sheffield, UK

[2]Department of Fluid Dynamics, A*Star Institute of High Performance Computing, 138632 Singapore

[3]Department of Mathematics, Imperial College London, SW7 2AZ London, UK

(Received 11 March 2016; revised 31 January 2017; accepted 8 February 2017;
first published online 15 March 2017)

The nonlinear response of a compressible boundary layer to unsteady free-stream vortical fluctuations of the convected-gust type is investigated theoretically and numerically. The free-stream Mach number is assumed to be of $O(1)$ and the effects of compressibility, including aerodynamic heating and heat transfer at the wall, are taken into account. Attention is focused on low-frequency perturbations, which induce strong streamwise-elongated components of the boundary-layer disturbances, known as streaks or Klebanoff modes. The amplitude of the disturbances is intense enough for nonlinear interactions to occur within the boundary layer. The generation and nonlinear evolution of the streaks, which acquire an $O(1)$ magnitude, are described on a self-consistent and first-principle basis using the mathematical framework of the nonlinear unsteady compressible boundary-region equations, which are derived herein for the first time. The free-stream flow is studied by including the boundary-layer displacement effect and the solution is matched asymptotically with the boundary-layer flow. The nonlinear interactions inside the boundary layer drive an unsteady two-dimensional flow of acoustic nature in the outer inviscid region through the displacement effect. A close analogy with the flow over a thin oscillating airfoil is exploited to find analytical solutions. This analogy has been widely employed to investigate steady flows over boundary layers, but is considered herein for the first time for unsteady boundary layers. In the subsonic regime the perturbation is felt from the plate in all directions, while at supersonic speeds the disturbance only propagates within the dihedron defined by the Mach line. Numerical computations are performed for carefully chosen parameters that characterize three practical applications: turbomachinery systems, supersonic flight conditions and wind tunnel experiments. The results show that nonlinearity plays a marked stabilizing role on the velocity and temperature streaks, and this is found to be the case for low-disturbance environments such as flight conditions. Increasing the free-stream Mach number inhibits the kinematic fluctuations but enhances the thermal streaks, relative to the free-stream velocity and temperature respectively, and the overall effect of nonlinearity becomes weaker. An abrupt deviation of the nonlinear solution from the linear one is observed in the case pertaining to a supersonic wind tunnel. Large-amplitude thermal streaks and the strong abrupt stabilizing effect of nonlinearity are two new features of supersonic flows. The present study provides an accurate

† Email address for correspondence: e.marensi@sheffield.ac.uk

signature of nonlinear streaks in compressible boundary layers, which is indispensable for the secondary instability analysis of unsteady streaky boundary-layer flows.

Key words: compressible boundary layers, transition to turbulence

1. Introduction

The transition from a laminar to a turbulent state in boundary layers, although studied for over a century, still represents one of the outstanding unsolved problems in fluid mechanics. A thorough understanding of the physics underlying this phenomenon is of great importance from a fundamental as well as from a practical point of view. The wall shear stress and heat transfer characteristics change dramatically depending on the flow regime being laminar, transitional or turbulent. Therefore, quantitative prediction and control of transition play a decisive role in determining the operating conditions and performance of flows around high-speed airfoils in a variety of industrial applications. Relevant examples are commercial and high-speed aircraft, space capsule re-entry into the atmosphere and flows around turbine stator vanes or rotor blades.

Boundary-layer transition is known to be strongly influenced by disturbances present in the oncoming stream, which penetrate into the boundary layer and eventually lead to the breakdown of the laminar flow. Such perturbations consist of acoustic (pressure), kinematic (vortical) and entropy (temperature) fluctuations, and may exist independently of each other when they are of sufficiently small amplitude.

In this paper we are concerned with free-stream vortical perturbations whose intensities are high enough ($Tu = 1\,\%$ or more, where Tu is the root-mean-square value of the velocity fluctuations) for transition to occur rather early, bypassing the so-called orderly route via viscous Tollmien–Schlichting (T–S) waves. In this scenario, referred to as bypass transition (Morkovin 1984), the laminar boundary-layer breakdown is preceded and caused by unsteady streamwise-elongated regions of high and low streamwise velocity. These structures have been referred to as breathing modes (Taylor 1939) because of their resemblance to a thickening and thinning of the layer, Klebanoff modes (Kendall 1985) after the experiments of Klebanoff (1971), or laminar streaks. The focus of our work is on the generation and nonlinear evolution of streaks in the compressible regime because in high-speed flows transition occurs more frequently through the bypass route than via the T–S wave growth described by the classical stability theory.

1.1. *Experiments and direct numerical simulations*

Experimental works (Arnal & Juillen 1978; Kendall 1985, 1990, 1991; Westin *et al.* 1994, 1998; Matsubara & Alfredsson 2001; Fransson, Matsubara & Alfredsson 2005) and direct numerical simulations (DNS) using realistic free-stream disturbances (Nagarajan, Lele & Ferziger 2007; Ovchinnikov, Choudhari & Piomelli 2008; Brinkerhoff & Yaras 2015) have provided an overall picture of bypass transition induced by free-stream turbulence in the incompressible regime. The reader is also referred to DNS studies (e.g. Jacobs & Durbin 2001; Brandt, Schlatter & Henningson 2004; Zaki & Durbin 2005) using inflow conditions synthesized through the continuous modes of the Orr–Sommerfeld/Squire equations. Despite its importance

in high-speed aircraft design and turbomachinery applications, the literature available on bypass transition in compressible flows is more limited than for incompressible flows. Supersonic wind tunnel experiments (Laufer 1961; Kendall 1967; Pate & Schueler 1969; Schneider 2001) showed that the transition behaviour is dominated by the noise radiated from the turbulent boundary layers on the walls. Transition may occur earlier in laboratory experiments than in flight conditions because of the high levels of tunnel noise (Schneider 2001). This discrepancy prevents the direct use of laboratory data for high-speed vehicle design. Although most of the experimental studies in the last few decades have focussed on acoustic disturbances, it should be recognized that more attention needs to be devoted to vortical disturbances. As speculated by Kendall (1975), at low speeds the tunnel sound might be less effective than other type of disturbances, such as the vortical fluctuations. In flight conditions vortical disturbances are the main source of perturbation influencing transition, while acoustic modes are weak and only become relevant at locations affected by the noise radiated by the engine.

Mayer, Von Terzi & Fasel (2011) performed DNS of the downstream development of a pair of oblique instability waves in a supersonic flat-plate boundary layer. They showed that transition in supersonic two-dimensional boundary layers can be initiated by very low disturbance levels (e.g. less than 0.01 %), which explains the practical relevance of the oblique breakdown mechanism for quiet environment such as free flight. Joo & Durbin (2012) carried out DNS of the transition initiated by discrete instability modes and continuous vortical modes in a Mach 4.5 boundary layer. As in Jacobs & Durbin (2001) and Zaki & Durbin (2005), their approach consisted of specifying the inflow conditions in terms of a superposition of the continuous spectra of the Orr–Sommerfeld and Squire operators. Such a practice has been questioned by Dong & Wu (2013) and Wu & Dong (2016), who showed that continuous spectra exhibit non-physical features (i.e. entanglement of Fourier components and abnormal size of the streamwise free-stream velocity) because non-parallel flow effects in the boundary layer are neglected. Non-parallelism actually plays a leading-order role in the entrainment of free-stream vortical disturbances into the boundary layer.

1.2. *Theoretical works*

In order to include the interaction between free-stream disturbances and the boundary layer, a rigorous mathematical formulation has been developed by Goldstein and co-workers (Goldstein, Leib & Cowley 1992; Goldstein & Leib 1993; Goldstein 1997; Wundrow & Goldstein 2001). Goldstein's theory is based on the boundary-region equations (Kemp 1951), which are the rigorous asymptotic limit of the Navier–Stokes equations for low-frequency and long-wavelength perturbations. For these disturbances, the streamwise derivatives in the viscous and pressure gradient terms are negligible, while the spanwise viscous diffusion is retained. In the limit of small-amplitude disturbances or short downstream distance, the boundary-region equations can be linearized about the Blasius solution. Leib, Wundrow & Goldstein (1999) used the linearized unsteady boundary-region equations (LUBR) to investigate the response of an incompressible laminar boundary layer to free-stream unsteady vortical fluctuations of the convected-gust type. Wu & Choudhari (2003) and Wu & Luo (2003) studied the instability of a Blasius boundary layer in the presence of steady and unsteady streaks, and showed that inviscid instability may occur when the distortion of the Klebanoff modes reaches a certain threshold value.

The linear analysis of Leib *et al.* (1999) was extended by Ricco, Luo & Wu (2011) to include nonlinear effects. Nonlinearity was found to attenuate the amplification of

the streaks and to distort the mean-flow profile significantly. A secondary instability analysis was carried out on the nonlinear streaks, proving that the streaky boundary layer may become inviscidly unstable during certain phases of the time modulation.

Ricco & Wu (2007) extended the incompressible analysis by Leib *et al.* (1999) to the compressible case and explained the formation and growth of thermal streaks, which are thought to play a significant role in the secondary instability. Ricco, Tran & Ye (2009) and Ricco, Shah & Hicks (2013) further studied the influence of wall heat transfer and wall suction, respectively, on the thermal streaks. The boundary-layer signature in the region relatively close to the leading edge corresponds to the inhomogeneous solution forced by the free-stream disturbance. However, Ricco & Wu (2007) also observed that sufficiently downstream exponentially growing disturbances are formed. For high subsonic and supersonic Mach numbers, the appearance of the amplifying disturbances was in the streamwise region of practical interest. Ricco & Wu (2007) showed that the growing disturbances evolved from the so-called quasi-three-dimensional Lam–Rott eigensolutions, which are excited by the free-stream disturbance and may be identified as highly oblique low-frequency T–S waves in the so-called first-mode family (Mack 1975, 1984). Ricco *et al.* (2009) found that wall cooling suppresses the streaks and enhances the growth of the instability waves.

The parabolized-stability equations (PSE) approach has been developed and used to study the evolution of instability modes in compressible boundary layers (see e.g. Chang *et al.* 1991). This methodology is based on the assumption that the base flow varies slowly in the streamwise direction and thus a Wentzel–Kramers–Brillouin (WKB) type of analysis is employed to parabolize the Navier–Stokes equations. The method requires, however, an *ad hoc* iterative procedure to identify a local streamwise wavenumber, and, furthermore, the presence of the streamwise pressure gradient causes some numerical instability due to a residual ellipticity in the equations (Li & Malik 1996). Neither of these problems occurs in the boundary-region equation approach because the local streamwise wavenumber tends to zero in the low-frequency asymptotic limit, and the equations are strictly parabolic. It should be pointed out that what we referred to as the boundary-region equation approach consists of appropriate initial (upstream) and boundary conditions, which correctly describe the entrainment of physically realizable free-stream disturbances. This is in contrast to the so-called optimal perturbation theory (Andersson, Berggren & Henningson 1999; Zuccher, Bottaro & Luchini 2006), which uses the adjoint of the boundary-region equations or of the PSE to find the initial (upstream) disturbances that undergo the maximum gain when evolving to a pre-selected streamwise location. Free-stream disturbances, the very factor causing bypass transition, are not taken into account in the latter formulation.

1.3. *Objectives*

As in the incompressible case, bypass transition in compressible boundary layers is of relevance for engineering applications, but it is also challenging theoretically because of the difficult mathematics involved and the complex physical mechanisms at play. As an essential step towards understanding and predicting compressible bypass transition, we formulate a rigorous description of the formation and nonlinear development of the unsteady compressible streaks induced by free-stream vortical fluctuations. Such a mathematical theory for compressible disturbances responsible for bypass transition is still absent. A further goal is to explain the nonlinear interactions between the

free-stream flow and the viscous boundary-layer flow, which occur through the displacement effect.

In § 2, the mathematical formulation and the scalings adopted are presented. In § 2.1 the free-stream perturbation is described and in § 2.2 the nonlinear unsteady compressible boundary-region equations are derived. In § 2.3 the outer-flow solution is obtained and matched with the inner solution in § 2.4. The numerical procedure to solve the boundary-region problem is outlined in § 3. The outer-flow velocity and pressure fields are shown in § 4 for the subsonic and supersonic regimes. In § 5.1 three different cases are considered, i.e. a turbomachinery flow (§ 5.1.1), a free flight flow (§ 5.1.2) and a supersonic wind tunnel flow (§ 5.1.3). The relevant results for the unsteady compressible streaks are presented in §§ 5.2 and 5.3. A summary and conclusions are given in § 6.

2. Formulation: scalings and governing equations

An air flow with a mean uniform velocity U^*_∞ and constant temperature T^*_∞ is considered; hereinafter, the symbol * is used to indicate dimensional quantities. Superimposed on the mean flow are homogeneous, statistically stationary turbulent vortical fluctuations, which are of the convected-gust type, i.e. they are passively advected by U^*_∞. The oncoming flow is considered isentropic and air is treated as a perfect gas. The speed of sound in the free stream is:

$$a^*_\infty = \sqrt{\gamma \mathcal{R}^* T^*_\infty}, \tag{2.1}$$

where $\gamma = 1.4$ is the ratio of the specific heats and $\mathcal{R}^*$ is the universal gas constant ($\mathcal{R}^* = 287.05$ N m kg^{-1} K^{-1}). The Mach number is defined as

$$M_\infty \equiv \frac{U^*_\infty}{a^*_\infty} = O(1). \tag{2.2}$$

In the Cartesian coordinate system employed to describe the flow, a point is represented by a position vector $\boldsymbol{x}^* = x^*\boldsymbol{i} + y^*\boldsymbol{j} + z^*\boldsymbol{k}$, where x^*, y^* and z^* define the streamwise, wall-normal and spanwise directions, respectively. The spatial coordinates are non-dimensionalized by a suitable reference length scale λ^*, which we shall specify below. The velocity and temperature reference scales are U^*_∞ and T^*_∞. The fluid properties, such as the density ρ^* and the dynamic viscosity μ^*, are scaled by their respective constant free-stream values, ρ^*_∞ and μ^*_∞. The time t^* and the pressure p^* are non-dimensionalized by λ^*/U^*_∞ and $\rho^*_\infty U^{*2}_\infty$, respectively.

It should be pointed out that in the supersonic regime shocks appear when the aerodynamic body (including a flat plate) has a finite thickness, and that at sufficiently high Mach numbers shocks can also arise for the idealized case of a flat plate with zero thickness due to the significant displacement produced by the viscous boundary-layer motion near the leading edge. The presence of a shock may change the boundary-layer instability properties if it is sufficiently close to the boundary layer (Chang, Malik & Hussaini 1990; Cowley & Hall 1990). Moreover, when any of the three types of perturbations, e.g. a vortical fluctuation, interacts with a shock, all three disturbances may appear downstream of the shock (McKenzie & Westphal 1968). The acoustic and entropy perturbations may influence transition via receptivity mechanisms (Fedorov & Khokhlov 2003; Zhong & Wang 2012; Qin & Wu 2016). In the present study, effects of shocks are neglected on the grounds that the plate is sufficiently thin and the Mach number is moderate so that shocks are weak and distant from the boundary. In this case, the interaction of unsteady disturbances with

the shock is decoupled from their subsequent interaction with the boundary layer (Qin & Wu 2016). The response of the boundary layer to each type of free-stream disturbance downstream of a shock can be analysed separately.

2.1. *Free-stream disturbances and scaling*

Free-stream turbulence is in general of broadband nature. For simplicity, we consider the case of vortical perturbation consisting of a pair of vortical modes with the same frequency (and hence streamwise wavenumber), but opposite spanwise wavenumber $\pm k_z^*$. In the incompressible analysis of Ricco *et al.* (2011), this choice of free-stream disturbance has led to good quantitative agreement between the theoretical prediction and wind tunnel experimental data. A similar behaviour is expected in the compressible case. The formulation and computation can be extended to realistic free-stream perturbations, which are of broadband nature as was shown by Zhang *et al.* (2011) for incompressible flows.

The velocity field of free-stream convected gusts of the assumed form can be expressed as

$$\boldsymbol{u}-\boldsymbol{i}=\epsilon\boldsymbol{u}_\infty(x-t,y,z)=\epsilon\left(\hat{\boldsymbol{u}}_+^\infty \mathrm{e}^{\mathrm{i}k_z z}+\hat{\boldsymbol{u}}_-^\infty \mathrm{e}^{-\mathrm{i}k_z z}\right)\mathrm{e}^{\mathrm{i}k_x(x-t)+\mathrm{i}k_y y}+\text{c.c.}, \tag{2.3}$$

where $\hat{\boldsymbol{u}}_\pm^\infty=\{\hat{u}_{x,\pm}^\infty,\hat{u}_{y,\pm}^\infty,\hat{u}_{z,\pm}^\infty\}=O(1)$ is a real vector, $\epsilon\ll 1$ is a measure of the free-stream perturbation level and c.c. indicates the complex conjugate. From the continuity equation, it follows that

$$k_x\hat{u}_{x,\pm}^\infty+k_y\hat{u}_{y,\pm}^\infty\pm k_z\hat{u}_{z,\pm}^\infty=0. \tag{2.4}$$

It is appropriate and convenient to take $\lambda^*=1/k_z^*$, so that $k_z=1$. The characteristic Reynolds number is

$$R_\lambda\equiv\frac{U_\infty^*\lambda^*}{\nu_\infty^*}\gg 1. \tag{2.5}$$

Only the components of the free-stream disturbance with $k_x\ll 1$ are considered as they have been shown in experiments to be the ones that can penetrate the most into the boundary layer to form streaks.

According to the result of Leib *et al.* (1999), the velocity perturbation is maximum when $x=O(k_x^{-1})$. The following scaling is thus introduced:

$$\bar{x}\equiv k_x x=O(1). \tag{2.6}$$

As a measure of the ratio between the boundary-layer thickness δ^* and the spanwise length scale λ^* at $\bar{x}=O(1)$, a scaled spanwise wavenumber is defined as

$$\kappa\equiv\frac{1}{\lambda^*}\sqrt{\frac{\lambda_x^*\nu_\infty^*}{2\pi U_\infty^*}}=\frac{k_z}{\sqrt{k_x R_\lambda}}. \tag{2.7}$$

The interest is in the downstream viscous region where $\delta^*=O(\lambda^*)$ so that viscous diffusion effects in the spanwise and wall-normal directions are comparable. This occurs at streamwise locations $x^*=O(\lambda^* R_\lambda)$, which, together with (2.6), leads to $k_x=O(R_\lambda^{-1})$, or, equivalently, $\kappa=O(1)$. As shown by Leib *et al.* (1999), $O(\epsilon)$ free-stream disturbances can produce $O(\epsilon/k_x)$ fluctuations of the streamwise velocity component within the boundary layer. Nonlinear effects become of leading order when $\epsilon/k_x=O(1)$, i.e. when the turbulent Reynolds number

$$r_t\equiv\epsilon R_\lambda=O(1), \tag{2.8}$$

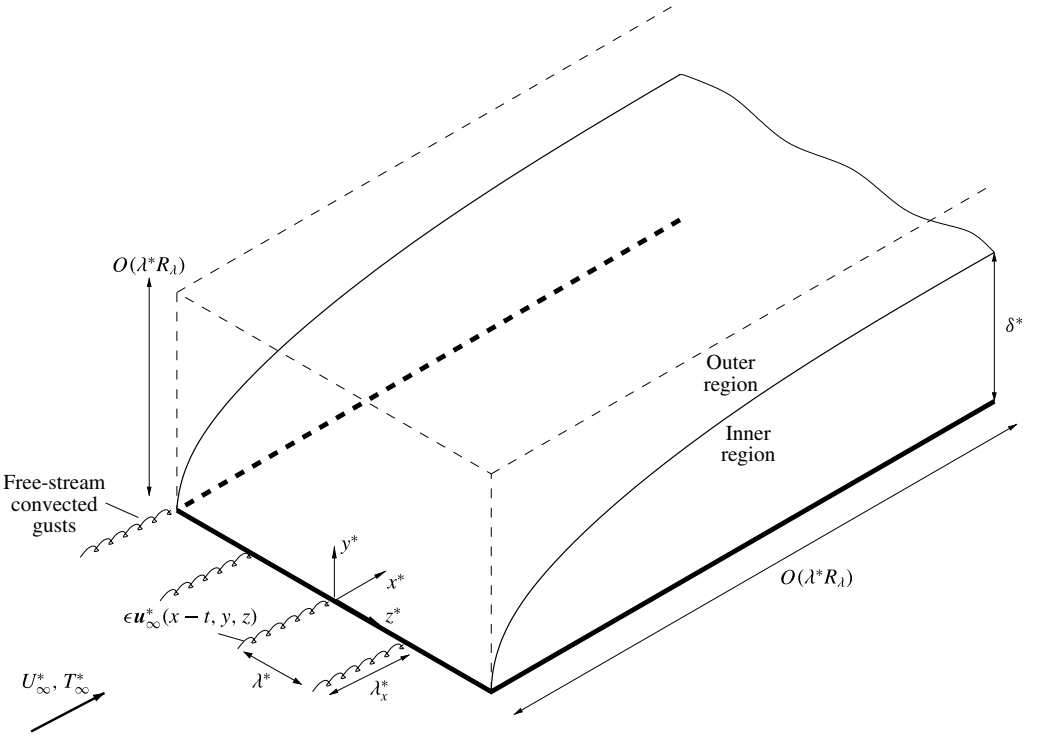

FIGURE 1. Sketch of the flow configuration representing the asymptotic regions (adapted from Leib *et al.* 1999).

since $k_x = O(R_\lambda^{-1})$. A schematic illustration of the flow domain and its asymptotic structure is shown in figure 1.

2.2. *The inner region: nonlinear unsteady compressible streaks*

In the boundary layer the solution is expressed as the superimposition of the unsteady perturbation on the steady laminar compressible boundary layer. The velocities and temperature of the Blasius flow have the similarity solution (Stewartson 1964)

$$\{U, V\} = \left\{ F'(\eta), \frac{T(\eta_c F' - F)}{\sqrt{2xR_\lambda}} \right\}, \quad T = T(\eta), \tag{2.9a,b}$$

where the prime indicates differentiation with respect to the similarity variable η,

$$\eta \equiv \sqrt{\frac{R_\lambda}{2x}} \int_0^y \rho(x, \check{y})\, \mathrm{d}\check{y}, \tag{2.10}$$

and $\eta_c = T^{-1} \int_0^\eta T(\check{\eta})\, \mathrm{d}\check{\eta}$. The x-momentum and the energy equations are:

$$FF'' + \left(\frac{\mu}{T} F''\right)' = 0, \tag{2.11a}$$

$$\left(\frac{\mu T'}{T}\right)' + PrFT' + Pr(\gamma - 1) M_\infty^2 \frac{\mu}{T} F''^2 = 0, \tag{2.11b}$$

where the Prandtl number $Pr = 0.7$. The system is subject to the boundary conditions,

$$F(0) = F'(0) = 0, \quad T(0) = T_w, \tag{2.12a,b}$$

$$F' \to 1, \quad T \to 1 \quad \text{as } \eta \to \infty, \tag{2.13a,b}$$

where T_w is the imposed wall temperature (isothermal condition). For $\eta \gg 1$, $F \to \bar{\eta} \equiv \eta - \beta_c$, where β_c depends on M_∞. Using the equation of state, the density ρ is given by

$$\rho = \frac{1}{T}. \tag{2.14}$$

The viscosity $\mu = \mu(T)$ is assumed to follow a power law,

$$\mu = T^\omega \quad \text{with } \omega = 0.76. \tag{2.15}$$

This relation has been proved to be more appropriate than the linear Chapman law ($\omega = 1$) in the Mach number range of interest $M_\infty < 4$ (Stewartson 1964).

The total boundary-layer flow is decomposed as the sum of the Blasius flow and the perturbation induced by the free-stream disturbance, namely,

$$\{u_{tot}, v_{tot}, w_{tot}, p_{tot}, \tau_{tot}\} = \left\{U, V, 0, -\frac{1}{2}, T\right\} + r_t \left\{\bar{u}(\bar{x}, \eta, z, t), \sqrt{\frac{2\bar{x}k_x}{R_\lambda}}\bar{v}(\bar{x}, \eta, z, t), \right.$$
$$\left. \frac{k_x}{k_z}\bar{w}(\bar{x}, \eta, z, t), \frac{k_x}{R_\lambda}\bar{p}(\bar{x}, \eta, z, t), \bar{\tau}(\bar{x}, \eta, z, t)\right\}, \tag{2.16}$$

where τ_{tot} stands for the temperature. The Blasius flow does not correspond to the mean flow; the latter also consists of the time-independent components generated by the nonlinear interactions, which are included in the perturbation. The scaling (2.8) and the decomposition (2.16) indicate that for low-frequency free-stream disturbances with spanwise wavelength comparable with the boundary-layer thickness and streamwise wavelength of $O(\lambda^* R_\lambda)$, the streamwise velocity and the temperature of the induced streaks acquire an amplitude of $O(\epsilon R_\lambda)$, which is much larger than $O(\epsilon)$ transverse velocity components (and the intensity of free-stream disturbances). The boundary-layer signature therefore bears all hallmarks of streaks observed in experiments. For the assumed simple composition of free-stream disturbance, the seeded oblique-mode pair would be dominant in the earlier stage, and is expected to remain the most significant in the nonlinear stage downstream. However, nonlinear interactions generate harmonics and the mean-flow distortion. The disturbance can be expressed as a Fourier series in time and z,

$$\{\bar{u}, \bar{v}, \bar{w}, \bar{p}, \bar{\tau}\} = \sum_{m,n} \left\{\hat{u}_{m,n}, \hat{v}_{m,n}, \hat{w}_{m,n}, \hat{p}_{m,n}, \hat{\tau}_{m,n}\right\} \mathrm{e}^{\mathrm{i}mk_x t + \mathrm{i}nk_z z}, \tag{2.17}$$

where $\{\hat{u}_{m,n}, \hat{v}_{m,n}, \hat{w}_{m,n}, \hat{p}_{m,n}, \hat{\tau}_{m,n}\}$ are functions of $\bar{x}$ and η. Unless otherwise specified, hereinafter the upper and lower limits of the summations are $\pm\infty$. As the physical quantities are real, the Fourier coefficients are Hermitian,

$$\hat{q}_{-m,-n} = \hat{q}^\star_{m,n}, \tag{2.18}$$

where $\hat{q}$ indicates any of $\{\hat{u}, \hat{v}, \hat{w}, \hat{p}, \hat{\tau}\}$ and the symbol * denotes the complex conjugate. The total density is decomposed as $\rho_{tot} = \rho + r_t\bar{\rho}$, where ρ is given

by (2.14). Substituting the total flow into the equation of state, one finds

$$\bar{\rho} = \frac{\gamma M_\infty^2 k_x}{T R_\lambda}\bar{p} - \frac{\bar{\tau}}{T^2} - r_t\frac{\bar{\rho}\bar{\tau}}{T}. \tag{2.19}$$

It follows that the total density is:

$$\rho_{tot} = \frac{1}{T} + r_t\left(\frac{\gamma M_\infty^2 k_x}{T R_\lambda}\bar{p} - \frac{\bar{\tau}}{T^2}\right) - r_t^2\frac{\bar{\rho}\bar{\tau}}{T}. \tag{2.20}$$

The total viscosity is expressed by applying (2.15) to the total flow and by expanding it using the binomial formula as

$$\mu_{tot} = (T + r_t\bar{\tau})^\omega = \sum_{j=0}^{\infty}\frac{(\omega)_j}{j!}T^{\omega-j}r_t^{\,j}\bar{\tau}^j = \mu + r_t\mu'\bar{\tau} + r_t^2\bar{\mu}, \tag{2.21}$$

where $(\omega)_j = \omega(\omega-1)(\omega-2)\ldots(\omega-j+1)$, $\mu' = \mathrm{d}\mu/\mathrm{d}T$ and $\bar{\mu}$ is the nonlinear part of the viscosity perturbation, which is decomposed as

$$\bar{\mu} = \sum_{m,n}\hat{\mu}_{m,n}(\bar{x},\eta)\mathrm{e}^{\mathrm{i}mk_x t + \mathrm{i}nk_z z}. \tag{2.22}$$

The nonlinearity of the viscosity comes from the power law exponent $\omega \neq 1$ and the turbulent Reynolds number $r_t = O(1)$. The nonlinear part $\bar{\mu}$ is null when either (i) $\omega = 1\,\forall\, r_t$ or (ii) $r_t = 0\,\forall\omega$ in (2.21). As long as $|r_t\bar{\tau}| < 1$, which applies to all the cases considered, the series in (2.21) is absolutely convergent.

By inserting (2.16) and (2.17) into the continuity, momentum and energy equations, using (2.20)–(2.22), and taking the limits $k_x \ll k_z$, $R_\lambda \gg 1$ with $k_x R_\lambda = O(1)$, the nonlinear unsteady compressible boundary-region equations are found as follows.

The continuity equation

$$\begin{aligned}&\frac{\eta_c}{2\bar{x}}\frac{T'}{T}\hat{u}_{m,n} + \frac{\partial\hat{u}_{m,n}}{\partial\bar{x}} - \frac{\eta_c}{2\bar{x}}\frac{\partial\hat{u}_{m,n}}{\partial\eta} - \frac{T'}{T^2}\hat{v}_{m,n} + \frac{1}{T}\frac{\partial\hat{v}_{m,n}}{\partial\eta} + \mathrm{i}n\hat{w}_{m,n} - \left(\frac{\mathrm{i}m}{T} + \frac{FT'}{2\bar{x}T^2}\right)\hat{\tau}_{m,n}\\ &\quad - \frac{F'}{T}\frac{\partial\hat{\tau}_{m,n}}{\partial\bar{x}} + \frac{F}{2\bar{x}T}\frac{\partial\hat{\tau}_{m,n}}{\partial\eta} = r_t\hat{\mathcal{C}}_{m,n},\end{aligned} \tag{2.23}$$

the x-momentum equation

$$\begin{aligned}&\left(\mathrm{i}m - \frac{\eta_c}{2\bar{x}}F'' + \kappa^2 n^2 T\mu\right)\hat{u}_{m,n} + F'\frac{\partial\hat{u}_{m,n}}{\partial\bar{x}} - \frac{1}{2\bar{x}}\left(F + \frac{\mu'T'}{T} - \frac{\mu T'}{T^2}\right)\frac{\partial\hat{u}_{m,n}}{\partial\eta} - \frac{\mu}{2\bar{x}T}\frac{\partial^2\hat{u}_{m,n}}{\partial\eta^2}\\ &\quad + \frac{F''}{T}\hat{v}_{m,n} + \left(\frac{FF'' - \mu'F''' - \mu''F''T'}{2\bar{x}T} + \frac{\mu'T'F''}{2\bar{x}T^2}\right)\hat{\tau}_{m,n} - \frac{\mu'F''}{2\bar{x}T}\frac{\partial\hat{\tau}_{m,n}}{\partial\eta} = r_t\hat{\mathcal{X}}_{m,n},\end{aligned} \tag{2.24}$$

the y-momentum equation

$$\begin{aligned}&\frac{1}{4\bar{x}^2}\left[FT + \eta_c(FT' - TF') - \eta_c^2F''T\right]\hat{u}_{m,n} + \frac{\mu'T'}{3\bar{x}}\frac{\partial\hat{u}_{m,n}}{\partial\bar{x}} - \frac{\mu}{6\bar{x}}\frac{\partial^2\hat{u}_{m,n}}{\partial\eta\partial\bar{x}}\\ &\quad + \frac{1}{12\bar{x}^2}\left(\mu + \eta_cT'\mu' - \frac{\mu T'\eta_c}{T}\right)\frac{\partial\hat{u}_{m,n}}{\partial\eta} + \frac{\eta_c\mu}{12\bar{x}^2}\frac{\partial^2\hat{u}_{m,n}}{\partial\eta^2}\end{aligned}$$

$$+\left(\mathrm{i}m+\frac{\eta_c}{2\bar{x}}F''+\frac{F'}{2\bar{x}}-\frac{FT'}{2\bar{x}T}+\kappa^2n^2\mu T\right)\hat{v}_{m,n}+F'\frac{\partial\hat{v}_{m,n}}{\partial\bar{x}}$$
$$-\frac{1}{\bar{x}}\left(\frac{F}{2}+\frac{2\mu'T'}{3T}-\frac{2\mu T'}{3T^2}\right)\frac{\partial\hat{v}_{m,n}}{\partial\eta}-\frac{2\mu}{3\bar{x}T}\frac{\partial^2\hat{v}_{m,n}}{\partial\eta^2}+\mathrm{i}n\frac{\mu'T'}{3\bar{x}}\hat{w}_{m,n}-\mathrm{i}n\frac{\mu}{6\bar{x}}\frac{\partial\hat{w}_{m,n}}{\partial\eta}$$
$$+\frac{1}{4\bar{x}^2}\left[\eta_c\left((FF')'-T\left(\frac{\mu'F''}{T}\right)'\right)-FF'-\frac{F^2T'}{T}-\mu'F''+\frac{4}{3}\left(\frac{\mu'T'F}{T}\right)'\right]\hat{\tau}_{m,n}$$
$$-\frac{\mu'F''}{2\bar{x}}\frac{\partial\hat{\tau}_{m,n}}{\partial\bar{x}}+\left(\frac{\mu'T'F}{3\bar{x}^2T}-\frac{\eta_c\mu'F''}{4\bar{x}^2}\right)\frac{\partial\hat{\tau}_{m,n}}{\partial\eta}+\frac{1}{2\bar{x}}\frac{\partial\hat{p}_{m,n}}{\partial\eta}=r_t\hat{\mathcal{Y}}_{m,n},\tag{2.25}$$

the z-momentum equation

$$\mathrm{i}n\kappa^2\frac{\eta_c\mu'T'T}{2\bar{x}}\hat{u}_{m,n}-\mathrm{i}n\kappa^2\frac{\mu T}{3}\frac{\partial\hat{u}_{m,n}}{\partial\bar{x}}+\mathrm{i}n\kappa^2\frac{\eta_c\mu T}{6\bar{x}}\frac{\partial\hat{u}_{m,n}}{\partial\eta}-\mathrm{i}n\kappa^2\mu'T'\hat{v}_{m,m}-\mathrm{i}n\kappa^2\frac{\mu}{3}\frac{\partial\hat{v}_{m,n}}{\partial\eta}$$
$$+\left(\mathrm{i}m+\frac{4n^2\kappa^2\mu T}{3}\right)\hat{w}_{m,n}+F'\frac{\partial\hat{w}_{m,n}}{\partial\bar{x}}-\frac{1}{2\bar{x}}\left(F+\frac{\mu'T'}{T}-\frac{\mu T'}{T^2}\right)\frac{\partial\hat{w}_{m,n}}{\partial\eta}$$
$$-\frac{\mu}{2\bar{x}T}\frac{\partial^2\hat{w}_{m,n}}{\partial\eta^2}-\frac{\mathrm{i}n\kappa^2FT'\mu'}{3\bar{x}}\hat{\tau}_{m,n}+\mathrm{i}n\kappa^2T\hat{p}_{m,n}=r_t\hat{\mathcal{Z}}_{m,n},\tag{2.26}$$

and the energy equation

$$-\frac{\eta_cT'}{2\bar{x}}\hat{u}_{m,n}-\frac{M_\infty^2(\gamma-1)\mu F''}{\bar{x}T}\frac{\partial\hat{u}_{m,n}}{\partial\eta}+\frac{T'}{T}\hat{v}_{m,n}$$
$$+\left[\mathrm{i}m+\frac{FT'}{2\bar{x}T}-\frac{1}{2Pr\bar{x}}\left(\frac{\mu'T'}{T}\right)'-\frac{M_\infty^2(\gamma-1)\mu'(F'')^2}{2\bar{x}T}+\frac{\mu n^2\kappa^2T}{Pr}\right]\hat{\tau}_{m,n}$$
$$+F'\frac{\partial\hat{\tau}_{m,n}}{\partial\bar{x}}-\frac{1}{2\bar{x}}\left(F+\frac{2\mu'T'}{PrT}-\frac{\mu T'}{PrT^2}\right)\frac{\partial\hat{\tau}_{m,n}}{\partial\eta}-\frac{\mu}{2Pr\bar{x}T}\frac{\partial^2\hat{\tau}_{m,n}}{\partial\eta^2}=r_t\hat{\mathcal{E}}_{m,n},\tag{2.27}$$

where the terms $\hat{\mathcal{C}}_{m,n}$, $\hat{\mathcal{X}}_{m,n}$, $\hat{\mathcal{Y}}_{m,n}$, $\hat{\mathcal{Z}}_{m,n}$, $\hat{\mathcal{E}}_{m,n}$ arise due to nonlinearity and are given in appendix A. The right-hand sides of (2.23)–(2.27), where the nonlinear terms are collected, vanish as $r_t\to 0$ so that the linearized compressible unsteady boundary-region equations of Ricco & Wu (2007) are recovered. Note that the above fully nonlinear equations are to be used to predict the entire development of streaks even though the disturbance evolves through a linear stage near the leading edge.

2.3. *The outer flow*

The outer-flow dynamics is influenced by the displacement of the underlying boundary-layer flow. The displacement effect becomes of leading order at downstream distances where $\bar{x}=O(1)$ and the streamwise velocity fluctuations acquire an $O(1)$ amplitude. The disturbance in the outer region consists of the three-dimensional vortical perturbation convected from upstream and of the two-dimensional disturbance arising from the boundary-layer displacement effect due to the nonlinear interactions in the boundary layer. The two-dimensional component attenuates over a wall-normal distance $O(\lambda^*R_\lambda)$, and thus depends on the relatively slow wall-normal variable $\bar{y}=k_xy=O(1)$. The three-dimensional component depends on y and, *a priori*, also on $\bar{y}$ because its governing equations involve the two-dimensional component as we

will discuss later. Following the approach of Wundrow & Goldstein (2001) and Ricco *et al.* (2011), the outer-region solution is expanded as:

$$\{u_{out}, v_{out}, w_{out}, p_{out}, \tau_{out}\} = \boldsymbol{Q} + \epsilon \bar{\boldsymbol{q}}_0(\bar{x}, \bar{y}, \bar{t}) + \epsilon \boldsymbol{q}_0(\bar{x}, y, \bar{y}, z, \bar{t}) + \epsilon^2 \boldsymbol{q}_1(\bar{x}, y, \bar{y}, z, \bar{t}) + \cdots, \tag{2.28}$$

where $\bar{t} \equiv k_x t = O(1)$, $\boldsymbol{Q}$ is the uniform mean flow, and $\bar{\boldsymbol{q}}_0$ and $\boldsymbol{q}_i$ $(i = 0, 1, \ldots)$ indicate the two-dimensional and three-dimensional disturbances, respectively.

2.3.1. *Linearized inviscid subsonic and supersonic flows*

The two-dimensional inviscid part of the perturbation is considered first: the subsonic and supersonic regimes are analysed by extending the approach of Ricco *et al.* (2011) to take compressibility into account. The transonic case is however beyond the scope of the present analysis. The two-dimensional terms $\{\bar{u}_0, \bar{v}_0, \bar{p}_0, \bar{\tau}_0, \bar{\rho}_0\}$ satisfy the linearized unsteady compressible Euler equations:

$$\frac{\partial \bar{u}_0}{\partial \bar{x}} + \frac{\partial \bar{v}_0}{\partial \bar{y}} + M_\infty^2 \left(\frac{\partial \bar{p}_0}{\partial \bar{t}} + \frac{\partial \bar{p}_0}{\partial \bar{x}} \right) = 0, \quad \frac{\partial \bar{u}_0}{\partial \bar{t}} + \frac{\partial \bar{u}_0}{\partial \bar{x}} + \frac{\partial \bar{p}_0}{\partial \bar{x}} = 0, \quad \frac{\partial \bar{v}_0}{\partial \bar{t}} + \frac{\partial \bar{v}_0}{\partial \bar{x}} + \frac{\partial \bar{p}_0}{\partial \bar{y}} = 0, \tag{2.29a–c}$$

where the density has been eliminated from the continuity equation by using the energy equation and the equation of state,

$$\frac{\partial \bar{\tau}_0}{\partial \bar{t}} + \frac{\partial \bar{\tau}_0}{\partial \bar{x}} - (\gamma - 1) M_\infty^2 \left(\frac{\partial \bar{p}_0}{\partial \bar{t}} + \frac{\partial \bar{p}_0}{\partial \bar{x}} \right) = 0, \quad \bar{\rho}_0 = \gamma M_\infty^2 \bar{p}_0 - \bar{\tau}_0. \tag{2.30a,b}$$

The displacement effect is associated with the transpiration velocity, i.e. the spanwise-averaged wall-normal velocity component at the boundary-layer outer edge. The continuity equation,

$$\frac{\partial \rho_{tot}}{\partial t} + \frac{\partial (\rho_{tot} u_{tot})}{\partial x} + \frac{\partial (\rho_{tot} v_{tot})}{\partial y} + \frac{\partial (\rho_{tot} w_{tot})}{\partial z} = 0, \tag{2.31}$$

is integrated first with respect to z over a spanwise period $\lambda_z = 2\pi/k_z$ and with respect to y from 0 to ∞. For the term $\partial(\rho_{tot} w_{tot})/\partial z$ a change in the order of integration is performed. At supersonic speeds this step is justified by the assumption that shock waves, if present, are of infinitesimal strength and therefore the flow remains smooth and isentropic. It follows that

$$\frac{1}{\lambda_z} \int_0^{\lambda_z} (\rho_{tot} v_{tot})|_{y \to \infty} \, \mathrm{d}z = -\frac{k_x}{\lambda_z} \left[\int_0^{\lambda_z} \int_0^{\infty} \frac{\partial (\rho_{tot} u_{tot})}{\partial \bar{x}} \, \mathrm{d}y \, \mathrm{d}z + \int_0^{\lambda_z} \int_0^{\infty} \frac{\partial \rho_{tot}}{\partial \bar{t}} \, \mathrm{d}y \, \mathrm{d}z \right]. \tag{2.32}$$

The first term on the right-hand side of (2.32) represents the derivative with respect to $\bar{x}$ of the spanwise-averaged boundary-layer displacement thickness, defined as

$$\bar{\delta}(\bar{x}, \bar{t}) = \frac{1}{\lambda_z} \int_0^{\lambda_z} \int_0^{\infty} [1 - (\rho_{tot} u_{tot})] \, \mathrm{d}y \, \mathrm{d}z. \tag{2.33}$$

The second term on the right-hand side of (2.32) is due to compressibility effects and is not present in Ricco *et al.* (2011). It can be written as the derivative with respect to $\bar{t}$ of a spanwise-averaged boundary-layer thickness $\bar{\delta}^c$ defined as

$$\bar{\delta}^c(\bar{x}, \bar{t}) = \frac{1}{\lambda_z} \int_0^{\lambda_z} \int_0^{\infty} (1 - \rho_{tot}) \, \mathrm{d}y \, \mathrm{d}z. \tag{2.34}$$

Matching the left-hand side of (2.32) with the outer flow gives

$$\frac{1}{\lambda_z}\int_0^{\lambda_z}(\rho_{tot}v_{tot})|_{y\to\infty}\,\mathrm{d}z=\frac{1}{\lambda_z}\int_0^{\lambda_z}(\rho_{out}v_{out})|_{\bar{y}\to 0}\,\mathrm{d}z=\epsilon\bar{v}_0, \tag{2.35}$$

where the terms $O(\epsilon^2)$ have been neglected. Therefore, equation (2.32) leads to

$$\bar{v}_0=\frac{k_x}{\epsilon}\left(\frac{\partial\bar{\delta}}{\partial\bar{x}}+\frac{\partial\bar{\delta}^c}{\partial\bar{t}}\right)\quad\text{as }\bar{y}\to 0, \tag{2.36}$$

where the compressibility effects appear in the definition of the displacement thickness $\bar{\delta}$ and in the additional term $\bar{\delta}^c$. Equation (2.36) is used as a boundary condition on the system (2.29).

The proof employed by Ricco *et al.* (2011) to show the irrotationality of the two-dimensional flow holds for the compressible case as long as the flow remains isentropic (i.e. shock waves are absent or, if present, their effect is negligible). Therefore, the potential $\bar{\phi}_0$ is introduced such that $\nabla_{\bar{x}\bar{y}}\bar{\phi}_0=\{\bar{u}_0,\ \bar{v}_0\}$, where $\nabla_{\bar{x}\bar{y}}$ denotes the gradient operator in the $\bar{x}$–$\bar{y}$ plane. By rewriting (2.29) in terms of $\bar{\phi}_0$ and eliminating the pressure from the continuity equation with the aid of the momentum equations, a single equation for the potential is derived,

$$\frac{\partial^2\bar{\phi}_0}{\partial\bar{y}^2}+(1-M_\infty^2)\frac{\partial^2\bar{\phi}_0}{\partial\bar{x}^2}-2M_\infty^2\frac{\partial^2\bar{\phi}_0}{\partial\bar{x}\partial\bar{t}}-M_\infty^2\frac{\partial^2\bar{\phi}_0}{\partial\bar{t}^2}=0,\quad M_\infty\neq 1, \tag{2.37}$$

which is a wave (i.e. hyperbolic) equation, indicating the acoustic nature of the perturbation. It is interesting that streaks emit sound waves spontaneously during their nonlinear evolution. Equation (2.37) is of the same form as the linearized perturbation velocity potential equation governing the flow over a thin airfoil performing small unsteady (periodic) oscillations in the transverse direction (refer to Landahl 1989, equation (1.7)). The small thickness of the airfoil is represented here by the boundary-layer displacement thickness, the equivalent body being semi-infinite rather than finite and closed (i.e. with null thickness at both ends of the body).

The problem of the flow over a thin oscillating airfoil has been widely studied in aeroelasticity because of the loads and vibrations occurring on the wing. Thanks to the linearization, two separated cases are distinguished: the thickness problem (symmetrical) and the lifting problem (anti-symmetrical). Aeroelasticians are usually interested in the latter because of the contribution to the lift experienced by the wing (Dowell 2014). Here it suffices to state that the analogy between the boundary-layer displacement effect and the thin airfoil theory only concerns the thickness problem, as circulatory flow is absent. This analogy was first suggested by Lighthill (1958) for incompressible flows and its use in the study of steady flows outside boundary layers has been well established (Van Dyke 1975). However, to the best of our knowledge, this analogy has never been considered for unsteady boundary layers.

By employing Fourier decomposition in time,

$$\bar{\phi}_0(\bar{x},\bar{y},\bar{t})=\sum_m\hat{\phi}_m(\bar{x},\bar{y})\mathrm{e}^{\mathrm{i}m\bar{t}}, \tag{2.38}$$

equation (2.37) is recast into a generalized Helmholtz differential equation (i.e. telegraph equation) for the Fourier coefficients $\hat{\phi}_m(\bar{x},\bar{y})$:

$$\frac{\partial^2\hat{\phi}_m}{\partial\bar{y}^2}+(1-M_\infty^2)\frac{\partial^2\hat{\phi}_m}{\partial\bar{x}^2}-2\mathrm{i}mM_\infty^2\frac{\partial\hat{\phi}_m}{\partial\bar{x}}+m^2M_\infty^2\hat{\phi}_m=0. \tag{2.39}$$

Performing the change $\hat{\phi}_m \to \hat{\Phi}_m$, where

$$\hat{\phi}_m(\bar{x}, \bar{y}) = \hat{\Phi}_m(\bar{x}, \bar{y})\mathrm{e}^{-b\bar{x}/2} \quad \text{with } b \equiv \frac{2\mathrm{i}mM_\infty^2}{M_\infty^2 - 1}, \quad M_\infty \neq 1, \tag{2.40}$$

the telegraph equation (2.39) is reduced to either the Helmholtz equation if $M_\infty < 1$ or the Klein–Gordon equation if $M_\infty > 1$:

$$|1 - M_\infty^2| \frac{\partial^2 \hat{\Phi}_m}{\partial \bar{x}^2} \pm \frac{\partial^2 \hat{\Phi}_m}{\partial \bar{y}^2} + \frac{m^2 M_\infty^2}{|1 - M_\infty^2|} \hat{\Phi}_m = 0, \tag{2.41}$$

where the $+$ or $-$ sign correspond to the subsonic or supersonic case, respectively. The appropriate boundary conditions for (2.41) are:

$$\frac{\partial \hat{\Phi}_m}{\partial \bar{y}} = \begin{cases} \dfrac{k_x}{\epsilon}(\hat{\delta}'_m + \mathrm{i}m\hat{\delta}^c_m)\mathrm{e}^{b\bar{x}/2}, & \bar{y} = 0, \bar{x} \geqslant 0, \\ 0, & \bar{y} = 0, \bar{x} < 0; \end{cases} \tag{2.42a}$$

$$\frac{\partial \hat{\Phi}_m}{\partial \bar{x}}, \frac{\partial \hat{\Phi}_m}{\partial \bar{y}} \text{ finite}, \quad \bar{x}^2 + \bar{y}^2 \to \infty, \tag{2.42b}$$

where $\hat{\delta}_m(\bar{x})$ and $\hat{\delta}^c_m(\bar{x})$ are the Fourier coefficients of $\bar{\delta}(\bar{x}, \bar{t})$, and $\bar{\delta}^c(\bar{x}, \bar{t})$ and the prime represents differentiation with respect to $\bar{x}$. Equation (2.42*a*) corresponds to the tangency (i.e. no penetration) condition imposed on a thin airfoil, according to which the velocity component normal to the body is fixed by the airfoil motion. This analogy has given rise to the well-known interpretation of the boundary-layer displacement effect as a surface distribution of sources (Lighthill 1958). The far-field boundary condition (2.42*b*) requires that the displacement-induced velocity field remains finite as the distance from the plate increases.

In the supersonic case it is convenient to solve for $\hat{\phi}_m$ directly. The fluid ahead of the body remains undisturbed and so the Laplace transform in the $\bar{x}$ direction can be employed,

$$\tilde{\phi}_m(s, \bar{y}) = \int_0^\infty \hat{\phi}_m(\bar{x}, \bar{y})\mathrm{e}^{-s\bar{x}}\,\mathrm{d}\bar{x}. \tag{2.43}$$

The telegraph equation (2.39) and the boundary condition (2.42*a*) for $\bar{x} \geqslant 0$ become:

$$\frac{\partial^2 \tilde{\phi}_m}{\partial \bar{y}^2} = c^2 \tilde{\phi}_m, \quad \frac{\partial \tilde{\phi}_m}{\partial \bar{y}}(s, 0) = \tilde{v}_m(s, 0), \tag{2.44a,b}$$

where $c^2 = s^2(M_\infty^2 - 1) + mM_\infty^2(2\mathrm{i}s - m)$ and $\tilde{v}_m(s, 0)$ indicates the Laplace transform of $\partial\hat{\phi}_m/\partial\bar{y}$ at $\bar{y} = 0$. The solution to (2.44) is

$$\tilde{\phi}_m(s, \bar{y}) = -\frac{\tilde{v}_m(s, 0)}{c}\mathrm{e}^{-c\bar{y}}, \quad \bar{y} \geqslant 0. \tag{2.45}$$

Inverting (2.45) and using the convolution theorem, one finds

$$\begin{aligned} \hat{\phi}_m(\bar{x}, \bar{y}; M_\infty > 1) \;=\; & -\frac{k_x}{\epsilon\sqrt{M_\infty^2 - 1}} \int_0^{\bar{x} - \bar{y}\sqrt{M_\infty^2 - 1}} \left[\hat{\delta}'_m(\bar{x}_0) + \mathrm{i}m\hat{\delta}^c_m(\bar{x}_0)\right] \mathrm{e}^{-(\mathrm{i}mM_\infty^2/(M_\infty^2 - 1))(\bar{x} - \bar{x}_0)} \\ & \times J_0\left[\frac{mM_\infty}{M_\infty^2 - 1}\sqrt{(\bar{x} - \bar{x}_0)^2 - \left(M_\infty^2 - 1\right)\bar{y}^2}\right] \mathrm{d}\bar{x}_0, \end{aligned} \tag{2.46}$$

where J_0 is the zeroth-order Bessel function of the first kind (Abramowitz & Stegun 1964). The procedure to derive (2.46) closely follows the theory proposed by Stewartson (1950) for harmonically oscillating thin airfoils in supersonic flows.

In the subsonic case, the disturbance is felt in all directions and so the use of the Laplace transform in $\bar{x}$ is not appropriate. The Fourier transform is instead employed and the analytic continuation of the Neumann boundary condition (2.42*a*) to the complex plane $\bar{\xi} = \bar{x} + \mathrm{i}\bar{y}$ is considered. The solution reads

$$\hat{\phi}_m(\bar{x}, \bar{y}; M_\infty < 1) = -\frac{\mathrm{i}k_x}{2\epsilon\sqrt{1-M_\infty^2}} \int_{\bar{x}-\mathrm{i}\bar{y}\sqrt{1-M_\infty^2}}^{\bar{x}+\mathrm{i}\bar{y}\sqrt{1-M_\infty^2}} \left[\hat{\delta}'_m(\bar{\xi}) + \mathrm{i}m\hat{\delta}^c_m(\bar{\xi})\right] \mathrm{e}^{(\mathrm{i}mM_\infty^2/(1-M_\infty^2))(\bar{x}-\bar{\xi})} \times J_0\left[\frac{mM_\infty}{1-M_\infty^2}\sqrt{\left(\bar{x}-\bar{\xi}\right)^2 + \left(1-M_\infty^2\right)\bar{y}^2}\right] \mathrm{d}\bar{\xi}. \tag{2.47}$$

The solution can also be expressed in terms of the Green's function by modelling the boundary-layer thickness as a distribution of pulsating sources as suggested by Lighthill's theory. The free-space Green's function associated with the Helmholtz equation (2.41) is given by Dragos (2004) on p. 33 for a single source located in the origin. Considering a line distribution of these sources at the point $(\bar{x}_0, 0)$, where $\bar{x}_0$ spans the $\bar{x}$ axis, and using the method of images to include the boundary $\bar{y} = 0$, we obtain

$$\hat{\phi}_m(\bar{x}, \bar{y}; M_\infty < 1) = \frac{\mathrm{i}k_x}{2\epsilon\sqrt{1-M_\infty^2}} \int_0^\infty \left[\hat{\delta}'_m(\bar{x}_0) + \mathrm{i}m\hat{\delta}^c_m(\bar{x}_0)\right] \mathrm{e}^{(\mathrm{i}mM_\infty^2/(1-M_\infty^2))(\bar{x}-\bar{x}_0)} \times H_0^{(2)}\left[\frac{mM_\infty}{1-M_\infty^2}\sqrt{(\bar{x}-\bar{x}_0)^2 + \left(1-M_\infty^2\right)\bar{y}^2}\right] \mathrm{d}\bar{x}_0, \tag{2.48}$$

where $H_0^{(2)}$ is the zeroth-order Hankel function of the second kind (Abramowitz & Stegun 1964). The solution with $H_0^{(2)}$ has been chosen instead of that with $H_0^{(1)}$ to ensure outgoing waves radiating from the source. As $M_\infty \to 0$, equation (2.47) matches the solution obtained in the incompressible case (Ricco *et al.* 2011):

$$\lim_{M_\infty \to 0} \hat{\phi}_m(\bar{x}, \bar{y}; M_\infty < 1) = -\frac{\mathrm{i}k_x}{2\epsilon} \int_{\bar{x}-\mathrm{i}\bar{y}}^{\bar{x}+\mathrm{i}\bar{y}} \hat{\delta}'_m(\xi)\,\mathrm{d}\xi = -\frac{\mathrm{i}k_x}{2\epsilon}[\hat{\delta}_m(\bar{x}+\mathrm{i}\bar{y}) - \hat{\delta}_m(\bar{x}-\mathrm{i}\bar{y})] = \frac{k_x}{\epsilon}\,\mathrm{Im}[\hat{\delta}_m(\bar{x}+\mathrm{i}\bar{y})], \tag{2.49}$$

where Im indicates the imaginary part and use has been made of the property of holomorphic functions, $\hat{\delta}_m(\bar{\xi}^\star) = \hat{\delta}_m(\bar{\xi})^\star$. The limit $M_\infty \to \infty$ is not considered because for very large hypersonic Mach numbers the Blasius boundary-layer assumption of negligible wall-normal pressure gradient is invalid (refer to Anderson 2006, p. 275).

The pressure is obtained from the y-momentum equation (2.29) as

$$\bar{p}_0 = -\left(\frac{\partial\bar{\phi}_0}{\partial\bar{t}} + \frac{\partial\bar{\phi}_0}{\partial\bar{x}}\right), \tag{2.50}$$

or, in Fourier space,

$$\hat{p}_m = -\left(\mathrm{i}m\hat{\phi}_m + \frac{\partial\hat{\phi}_m}{\partial\bar{x}}\right). \tag{2.51}$$

From substitution of the supersonic and subsonic expressions for the potential, equations (2.46) and (2.48), into (2.51), it follows that

$$\hat{p}_m(\bar{x},\bar{y};M_\infty>1)=\frac{k_x}{\epsilon\sqrt{M_\infty^2-1}}\left\{\int_0^{\bar{x}-\bar{y}\sqrt{M_\infty^2-1}} f(\bar{x}_0,\bar{x},\bar{y})\,\mathrm{d}\bar{x}_0 - \left[\hat{\delta}_m'(\bar{x}-\bar{y}\sqrt{M_\infty^2-1})+\mathrm{i}m\hat{\delta}_m^c(\bar{x}-\bar{y}\sqrt{M_\infty^2-1})\right]\mathrm{e}^{-(\mathrm{i}mM_\infty^2/\sqrt{M_\infty^2-1})\bar{y}}\right\} \tag{2.52}$$

in the supersonic case, where

$$\begin{aligned} f \;=\; & \left[\hat{\delta}_m'(\bar{x}_0)+\mathrm{i}m\hat{\delta}_m^c(\bar{x}_0)\right]\mathrm{e}^{-(\mathrm{i}mM_\infty^2/(M_\infty^2-1))(\bar{x}-\bar{x}_0)} \\ & \times\left\{\frac{\mathrm{i}m}{M_\infty^2-1}J_0\left[\frac{mM_\infty}{M_\infty^2-1}\sqrt{(\bar{x}-\bar{x}_0)^2-\left(M_\infty^2-1\right)\bar{y}^2}\right]\right. \\ & \left.+\frac{mM_\infty(\bar{x}-\bar{x}_0)}{(M_\infty^2-1)\sqrt{(\bar{x}-\bar{x}_0)^2-(M_\infty^2-1)\bar{y}^2}}J_1\left[\frac{mM_\infty}{M_\infty^2-1}\sqrt{(\bar{x}-\bar{x}_0)^2-\left(M_\infty^2-1\right)\bar{y}^2}\right]\right\} \end{aligned} \tag{2.53}$$

and J_1 is the first-order Bessel function of the first kind (Abramowitz & Stegun 1964), and in the subsonic case

$$\hat{p}_m(\bar{x},\bar{y};M_\infty<1) \;=\; \frac{\mathrm{i}k_x}{2\epsilon\sqrt{1-M_\infty^2}}\int_0^\infty g(\bar{x}_0,\bar{x},\bar{y})\,\mathrm{d}\bar{x}_0, \tag{2.54}$$

where

$$\begin{aligned} g \;=\; & \left[\hat{\delta}_m'(\bar{x}_0)+\mathrm{i}m\hat{\delta}_m^c(\bar{x}_0)\right]\mathrm{e}^{(\mathrm{i}mM_\infty^2/(1-M_\infty^2))(\bar{x}-\bar{x}_0)} \\ & \times\left\{\frac{\mathrm{i}m}{1-M_\infty^2}H_0^{(2)}\left[\frac{mM_\infty}{1-M_\infty^2}\sqrt{(\bar{x}-\bar{x}_0)^2+\left(1-M_\infty^2\right)\bar{y}^2}\right]\right. \\ & -\frac{mM_\infty\,(\bar{x}-\bar{x}_0)}{(1-M_\infty^2)\sqrt{(\bar{x}-\bar{x}_0)^2+(1-M_\infty^2)\bar{y}^2}} \\ & \left.\times H_1^{(2)}\left[\frac{mM_\infty}{1-M_\infty^2}\sqrt{(\bar{x}-\bar{x}_0)^2+(1-M_\infty^2)\bar{y}^2}\right]\right\}, \end{aligned} \tag{2.55}$$

and $H_1^{(2)}$ is the first-order Hankel function of the second kind (Abramowitz & Stegun 1964). The temperature is found from the energy equation (2.30) as

$$\bar{\tau}_0=(\gamma-1)M_\infty^2\bar{p}_0. \tag{2.56}$$

2.3.2. *Viscous three-dimensional flow*

By substituting the expansion (2.28) into the Navier–Stokes equations and subtracting the equations (2.29) and (2.30) for the displacement-induced disturbance, the leading-order three-dimensional part of the perturbation is found to satisfy the

equations:

$$\frac{\partial v_0}{\partial y} + \frac{\partial w_0}{\partial z} = 0, \tag{2.57}$$

$$\left\{ \frac{\partial}{\partial \bar{t}} + \frac{\partial}{\partial \bar{x}} + \frac{\epsilon}{k_x} \left[(\bar{v}_0 + v_0) \frac{\partial}{\partial y} + w_0 \frac{\partial}{\partial z} \right] \right\} \begin{Bmatrix} u_0 \\ v_0 \\ w_0 \\ \tau_0 \end{Bmatrix} = -\frac{\epsilon}{k_x} \begin{Bmatrix} 0 \\ \partial p_1/\partial y \\ \partial p_1/\partial z \\ 0 \end{Bmatrix} + \kappa^2 \nabla_{yz}^2 \begin{Bmatrix} u_0 \\ v_0 \\ w_0 \\ Pr^{-1}\tau_0 \end{Bmatrix}, \tag{2.58}$$

where $p_0 = 0$ without loss of generality and ∇_{yz} is the gradient operator in the y–z plane.

The three-dimensional part of the perturbation in (2.57) and (2.58) does not directly depend on the slow variable $\bar{y}$ at the leading order, but the momentum equations (2.58) include the inviscid wall-normal velocity component $\bar{v}_0$, which depends on $\bar{y}$. Therefore, the dependence of the leading-order three-dimensional disturbance upon $\bar{y}$ is parametric. The aim of the following analysis is to decouple (2.58) from $\bar{v}_0$ to obtain a system of equations in the only unknowns $\{u_0, v_0, w_0, \tau_0, p_1\}$. This is accomplished by introducing the Prandtl transformation, $\hat{y} = y - \mathrm{Re}[\Delta(\bar{\xi}, \bar{t})]$, where Re denotes the real part and Δ is suitably chosen to eliminate the coupling between $\{u_0, v_0, w_0, \tau_0, p_1\}$ and $\bar{v}_0$ from (2.58). The new variable $\hat{y}$ is written in this form for consistency with the previous analyses of Wundrow & Goldstein (2001) and Ricco *et al.* (2011), although it will turn out that only the dependence of Δ on the real variables $\bar{x}$ and $\bar{t}$ is relevant since we are interested in the matching at $\bar{y} = 0$. Written in terms of $\hat{y}$, equations (2.57) and (2.58) become

$$\frac{\partial v_0}{\partial \hat{y}} + \frac{\partial w_0}{\partial z} = 0, \tag{2.59}$$

$$\mathcal{N} \begin{Bmatrix} u_0 \\ v_0 \\ w_0 \\ \tau_0 \end{Bmatrix} = -\frac{\epsilon}{k_x} \begin{Bmatrix} 0 \\ \partial p_1/\partial \hat{y} \\ \partial p_1/\partial z \\ 0 \end{Bmatrix} + \kappa^2 \nabla_{\hat{y}z}^2 \begin{Bmatrix} u_0 \\ v_0 \\ w_0 \\ Pr^{-1}\tau_0 \end{Bmatrix}, \tag{2.60}$$

where $\nabla_{\hat{y}z}$ is the gradient operator in the $\hat{y}$–z plane and $\mathcal{N}$ is the differential operator:

$$\mathcal{N} = \frac{\partial}{\partial \bar{t}} + \frac{\partial}{\partial \bar{x}} + \frac{\epsilon}{k_x} \left(v_0 \frac{\partial}{\partial \hat{y}} + w_0 \frac{\partial}{\partial z} \right) - \left(\mathrm{Re} \left[\frac{\partial \Delta}{\partial \bar{t}} + \frac{\partial \Delta}{\partial \bar{\xi}} \right] - \frac{\epsilon}{k_x} \bar{v}_0 \right) \frac{\partial}{\partial \hat{y}}. \tag{2.61}$$

The dependence on $\bar{v}_0$ is removed by choosing Δ to satisfy (Ricco *et al.* 2011)

$$\mathrm{Re} \left[\frac{\partial \Delta}{\partial \bar{t}} + \frac{\partial \Delta}{\partial \bar{\xi}} \right] = \frac{\epsilon}{k_x} \bar{v}_0, \tag{2.62}$$

which, in view of (2.36), becomes

$$\frac{\partial \Delta}{\partial \bar{t}} + \frac{\partial \Delta}{\partial \bar{x}} = \frac{\partial \bar{\delta}}{\partial \bar{x}} + \frac{\partial \bar{\delta}^c}{\partial \bar{t}} \quad \text{at } \bar{y} = 0. \tag{2.63}$$

Decomposing Δ into Fourier series as

$$\Delta\left(\bar{x}, \bar{t}\right) = \sum_m \hat{\Delta}_m(\bar{x}) \mathrm{e}^{-\mathrm{i}m(\bar{x} - \bar{t})} \quad \text{at } \bar{y} = 0, \tag{2.64}$$

and using the time Fourier series of $\bar{\delta}$ and $\bar{\delta}^c$, we obtain the expression for $\hat{\Delta}_m$,

$$\hat{\Delta}_m(\bar{x}) = \hat{\delta}_m(\bar{x})\mathrm{e}^{\mathrm{i}m\bar{x}} + \mathrm{i}m \int_0^{\bar{x}} \left[\hat{\delta}_m(\check{x}) - \hat{\delta}_m^c(\check{x})\right] \mathrm{e}^{\mathrm{i}m\check{x}}\,\mathrm{d}\check{x}, \quad \text{at } \bar{y} = 0, \tag{2.65}$$

where the condition $\Delta(0, \bar{t}) = 0,\ \forall \bar{t} > 0$ has been employed.

Equation (2.60) shows that the streamwise velocity u_0 and the temperature τ_0 are decoupled from the transverse velocities $\{v_0, w_0\}$ and from the pressure p_1. At leading order, only $\{v_0, w_0, p_1\}$ enter the matching with the boundary-layer solution, while the matching of $\{u_0, \tau_0\}$ needs to be considered when a solution with an order of accuracy higher than $O(R_\lambda^{-1})$ is sought.

In view of the continuity equation (2.59), the streamfunction $\psi_0(\bar{x}, \hat{y}, z, \bar{t})$ is introduced such that $\boldsymbol{\nabla}_{\hat{y}z}\psi_0 = \{-w_0, v_0\}$. In terms of the streamfunction the transverse momentum equations are recast into a transport equation for the longitudinal vorticity $\nabla^2_{\hat{y}z}\psi_0$,

$$\left[\frac{\partial}{\partial \bar{t}} + \frac{\partial}{\partial \bar{x}} + \frac{\epsilon}{k_x}\left(\frac{\partial \psi_0}{\partial z}\frac{\partial}{\partial \hat{y}} - \frac{\partial \psi_0}{\partial \hat{y}}\frac{\partial}{\partial \hat{z}}\right)\right] \nabla^2_{\hat{y}z}\psi_0 = \kappa^2 \nabla^4_{\hat{y}z}\psi_0, \tag{2.66}$$

along with the Poisson equation for the pressure,

$$\nabla^2_{\hat{y}z} p_1 = 2\left[\frac{\partial^2 \psi_0}{\partial \hat{y}^2}\frac{\partial^2 \psi_0}{\partial z^2} - \left(\frac{\partial^2 \psi_0}{\partial \hat{y}\partial z}\right)^2\right]. \tag{2.67}$$

In the general case of a full spectrum of free-stream vortical disturbances, the streamfunction is decomposed as:

$$\psi_0\left(\bar{x}, \hat{y}, z, \bar{t}\right) = \sum_{m,n,j} \hat{\psi}^{(j)}_{m,n}(\bar{x})\mathrm{e}^{\mathrm{i}(m\bar{t} + jk_y\hat{y} + nk_z z)}. \tag{2.68}$$

By substituting (2.68) into (2.66) and expanding the resulting equation for a pair of oblique forcing modes, the nonlinear terms cancel out and (2.66) reduces to

$$\left(\mathrm{i}m + \frac{\partial}{\partial \bar{x}}\right) \hat{\psi}^{(j)}_{m,n} = -\kappa^2 \left(j^2 k_y^2 + n^2 k_z^2\right) \hat{\psi}^{(j)}_{m,n}, \tag{2.69}$$

with $\{m, j, n\} = \{1, -1, \pm 1\}$. The solution is:

$$\hat{\psi}^{(-1)}_{1,\pm 1} = \mp \mathrm{i} c_\infty \mathrm{e}^{-\mathrm{i}\bar{x} - \kappa^2(k_y^2 + k_z^2)\bar{x}} + \text{c.c.}, \tag{2.70}$$

where $c_\infty = 1/k_y$ is chosen to normalize the amplitude of the free-stream spanwise velocity to unity. From (2.68) and (2.70) it follows that

$$\psi_0\left(\bar{x}, \hat{y}, z, \bar{t}\right) = -2\mathrm{i} c_\infty \cos(\bar{x} - \bar{t} + k_y\hat{y})\mathrm{e}^{-\kappa^2(k_y^2 + k_z^2)\bar{x} + \mathrm{i}k_z z} + \text{c.c.}. \tag{2.71}$$

The transverse velocities are obtained as

$$\{v_0, w_0\} = 2c_\infty \left\{k_z \cos(\bar{x} - \bar{t} + k_y\hat{y}),\ -\mathrm{i}k_y \sin(\bar{x} - \bar{t} + k_y\hat{y})\right\} \mathrm{e}^{-\kappa^2(k_y^2 + k_z^2)\bar{x} + \mathrm{i}k_z z} + \text{c.c.}. \tag{2.72}$$

By inserting (2.71) into (2.67), the pressure is found to be

$$p_1 = 2k_y^2 c_\infty^2 \mathrm{e}^{-2\kappa^2(k_y^2 + k_z^2)\bar{x} + 2\mathrm{i}k_z z} - 2k_z^2 c_\infty^2 \mathrm{e}^{-2\kappa^2(k_y^2 + k_z^2)\bar{x}} \cos(2\bar{x} - 2\bar{t} + 2k_y\hat{y}) + \text{c.c.}. \tag{2.73}$$

At $\bar{y}=0$, the expression $\hat{y}=y-\Delta(\bar{x},\bar{t})$ is substituted into (2.71)–(2.73), and the time-dependent terms are expanded into Fourier series,

$$\mathrm{e}^{\mathrm{i}\bar{t}+\mathrm{i}k_y\Delta(\bar{x},\bar{t})}=\sum_m \hat{\chi}_m(\bar{x})\mathrm{e}^{\mathrm{i}m\bar{t}},\quad \mathrm{e}^{2\mathrm{i}\bar{t}+2\mathrm{i}k_y\Delta(\bar{x},\bar{t})}=\sum_m \hat{\pi}_m(\bar{x})\mathrm{e}^{\mathrm{i}m\bar{t}}. \tag{2.74a,b}$$

Rewriting (2.72) and (2.73) with the aid of (2.74), the outer-flow solution for $y=O(1)$ is obtained as

$$\{v_0,\,w_0,\,p_1\}=\sum_{m,n}\left\{v^\dagger_{m,n},\,w^\dagger_{m,n},\,p^\dagger_{m,n}\right\}\mathrm{e}^{\mathrm{i}m\bar{t}+\mathrm{i}nk_z z}, \tag{2.75}$$

with

$$v^\dagger_{m,\pm1}=k_z c_\infty \mathrm{e}^{-\kappa^2(k_y^2+k_z^2)\bar{x}}\left[\hat{\chi}_m\mathrm{e}^{-\mathrm{i}(\bar{x}+k_y y)}+\hat{\chi}^\star_{-m}\mathrm{e}^{\mathrm{i}(\bar{x}+k_y y)}\right], \tag{2.76a}$$

$$w^\dagger_{m,\pm1}=\pm k_y c_\infty \mathrm{e}^{-\kappa^2(k_y^2+k_z^2)\bar{x}}\left[\hat{\chi}_m\mathrm{e}^{-\mathrm{i}(\bar{x}+k_y y)}-\hat{\chi}^\star_{-m}\mathrm{e}^{\mathrm{i}(\bar{x}+k_y y)}\right], \tag{2.76b}$$

$$p^\dagger_{0,\pm2}=2k_y^2c_\infty^2\mathrm{e}^{-2\kappa^2(k_y^2+k_z^2)\bar{x}}, \tag{2.76c}$$

$$p^\dagger_{m,0}=-2k_z^2c_\infty^2\mathrm{e}^{-2\kappa^2(k_y^2+k_z^2)\bar{x}}\left[\hat{\pi}_m\mathrm{e}^{-2\mathrm{i}(\bar{x}+k_y y)}+\hat{\pi}^\star_{-m}\mathrm{e}^{2\mathrm{i}(\bar{x}+k_y y)}\right]. \tag{2.76d}$$

The other components $v^\dagger_{m,n}$, $w^\dagger_{m,n}$ with $n\neq\pm1$ and $p^\dagger_{m,n}$ with $n\neq0,\,\pm2$ are null. Although the upstream flow is forced only by a pair of oblique modes with opposite spanwise wavenumbers, further downstream the disturbance is composed of all the temporal harmonics. These are generated by nonlinear interactions in the boundary layer and transmitted to the outer flow via the displacement effect. Although the Fourier components (2.76) are of the same form as those obtained in the incompressible case (refer to Ricco *et al.* 2011, equation (2.28)), the coefficients $\hat{\chi}_m$ and $\hat{\pi}_m$ defined in (2.74) now include the compressible effects, the function $\Delta(\bar{x},\bar{t})$ being related to δ and δ^c through (2.65).

2.4. *Initial and boundary conditions*

As the boundary-region equations (2.23)–(2.27) constitute a parabolic system in the streamwise direction, initial conditions are needed for $\bar{x}\ll1$. Since the velocity and temperature fluctuations are of small amplitude near the leading edge, their governing equations become linear. This was elucidated by Ricco *et al.* (2011), who showed that the full nonlinear regime develops gradually from the initial linear stage in the upstream region corresponding to $R_\lambda^{-1}\ll\bar{x}\ll1$. The initial conditions for the forced modes $(m,n)=(1,\pm1)$ are thus the same as those in Ricco & Wu (2007).

The upstream conditions are found by first seeking the power series solution for $\eta=O(1)$ and $\bar{x}\ll1$,

$$\{\bar{u},\,\bar{v},\,\bar{w},\,\bar{\tau},\,\bar{p}\}=\sum_{n=0}^{\infty}(2\bar{x})^{n/2}\left\{2\bar{x}U_n(\eta),\,V_n(\eta),\,W_n(\eta),\,2\bar{x}T_n(\eta),\,(2\bar{x})^{-1/2}P_n(\eta)\right\}, \tag{2.77}$$

and by constructing a composite solution that is valid for $\bar{x}\ll1$ and $\forall\eta$:

$$\{\hat{u},\,\hat{v},\,\hat{w},\,\hat{\tau},\,\hat{p}\}_{-1,\pm1}\to\pm\frac{\mathrm{i}\kappa^2}{k_z}u_{z,w,\pm}\left\{U_{in},\,V_{in},\,\mp\mathrm{i}W_{in},\,T_{in},\,P_{in}\right\}, \tag{2.78}$$

where $\{U_{in},\,V_{in},\,W_{in},\,T_{in},\,P_{in}\}$ are equal to the right-hand sides of equations (4.12)–(4.16) in Ricco & Wu (2007). The term $u_{z,w,\pm}$ represents the spanwise slip velocity at

the surface of the plate (refer to Leib *et al.* 1999, equation (3.14)). In the case of a pair of oblique modes, it is given by

$$u_{z,w,\pm} = \mp 1 \pm \frac{\mathrm{i}k_z}{\sqrt{k_x^2 + k_z^2}} \hat{u}^{\infty}_{y,\pm}. \tag{2.79}$$

For all the other harmonics generated by nonlinear effects, null initial velocity, temperature and pressure profiles are imposed.

The velocity fluctuations are required to vanish at the wall (no-slip condition). Two types of different thermal boundary conditions at the wall may be imposed: the Dirichlet boundary condition, $\bar{\tau}(0) = 0$, which was also employed by Ricco & Wu (2007), and the Neumann boundary condition, $\partial\bar{\tau}/\partial\eta|_{\eta=0} = 0$. The condition $\bar{\tau}(0) = 0$ is used herein as Ricco *et al.* (2009) showed that there is no substantial difference in the development of the Klebanoff modes.

As $\eta \to \infty$, the boundary-region solution must match to the limit $\bar{y} \to 0$ of the outer flow. On taking into account the decomposition (2.16) and (2.17) within the boundary layer, the matching with the outer solution (2.75) requires that

$$\left\{\hat{u}_{m,n}, \hat{v}_{m,n}, \hat{w}_{m,n}, \hat{p}_{m,n}, \hat{\tau}_{m,n}\right\} \to \left\{0, \frac{\kappa}{\sqrt{2\bar{x}}} v^{\dagger}_{m,n}, \kappa^2 w^{\dagger}_{m,n}, \frac{\epsilon}{k_x} p^{\dagger}_{m,n}, 0\right\} \quad \text{as } \eta \to \infty \tag{2.80}$$

for $\bar{x} = O(1)$, where the condition on $\hat{v}_{m,n}$ holds only for $n \neq 0$. In the spanwise-averaged equations ($n = 0$) the pressure only appears in the y-momentum equation. The velocities and the temperature are calculated by solving the continuity, x- and z-momentum and the energy equations. The condition on $\hat{v}_{m,0}$ as $\eta \to \infty$ is not needed because the order of the system has decreased. As an *a posteriori* check, the free-stream value of $\hat{v}_{m,0}$ is obtained from the large-η limit of the continuity equation,

$$\hat{v}_{m,0} = \frac{k_x}{\epsilon}\frac{\kappa}{\sqrt{2\bar{x}}}\left(\frac{\mathrm{d}\hat{\delta}_m}{\mathrm{d}\bar{x}} - \frac{\mathrm{d}\delta_{bl}}{\mathrm{d}\bar{x}} + \mathrm{i}m\hat{\delta}^c_m\right) \tag{2.81}$$

$$\begin{aligned} = &-\int_0^{\infty}\left(\frac{\partial\hat{u}_{m,0}}{\partial\bar{x}} + \frac{\hat{u}_{m,0}}{2\bar{x}}\right)\mathrm{d}\eta + \int_0^{\infty}\frac{F'}{T}\left(\frac{\partial\hat{\tau}_{m,0}}{\partial\bar{x}} + \frac{\hat{\tau}_{m,0}}{2\bar{x}}\right)\mathrm{d}\eta + \int_0^{\infty}\frac{\mathrm{i}m}{T}\hat{\tau}_{m,0}\mathrm{d}\eta \\ &- r_t\int_0^{\infty} T\left(\frac{\partial\widehat{\bar{\rho}\bar{u}}_{m,0}}{\partial\bar{x}} + \frac{\widehat{\bar{\rho}\bar{u}}_{m,0}}{2\bar{x}}\right)\mathrm{d}\eta + r_t\int_0^{\infty}\frac{\mathrm{i}m}{T}\widehat{\bar{\rho}\bar{\tau}}_{m,0}\,\mathrm{d}\eta \\ &+ r_t\int_0^{\infty} F'\left(\frac{\partial\widehat{\bar{\rho}\bar{\tau}}_{m,0}}{\partial\bar{x}} + \frac{\widehat{\bar{\rho}\bar{\tau}}_{m,0}}{2\bar{x}}\right)\mathrm{d}\eta \quad \text{as } \eta \to \infty, \end{aligned} \tag{2.82}$$

where δ_{bl} is the compressible Blasius displacement thickness,

$$\delta_{bl} = \int_0^{\infty}\left[1 - \frac{F'(\eta)}{T(\eta)}\right]\mathrm{d}y = \sqrt{\frac{2\bar{x}}{k_x R_\lambda}}(\gamma_c + \beta_c), \tag{2.83}$$

and $\gamma_c = \eta_c - \eta$ as $\eta \to \infty$. In the limit $M_\infty \to 0$ the result of Ricco *et al.* (2011) is recovered:

$$\hat{v}_{m,0} = \frac{k_x}{\epsilon}\frac{\kappa}{\sqrt{2\bar{x}}}\left(\frac{\mathrm{d}\hat{\delta}_m}{\mathrm{d}\bar{x}} - \frac{\mathrm{d}\delta_{bl}}{\mathrm{d}\bar{x}}\right) = -\int_0^{\infty}\left(\frac{\partial\hat{u}_{m,0}}{\partial\bar{x}} + \frac{\hat{u}_{m,0}}{2\bar{x}}\right)\mathrm{d}\eta \quad \text{as } \eta \to \infty, \tag{2.84}$$

where $\delta_{bl} = \int_0^\infty [1 - F'(\eta)]\,\mathrm{d}y = \beta\sqrt{2\bar{x}/k_x R_\lambda}$ is the incompressible Blasius displacement thickness and $\beta = 1.2168$. In the compressible case the additional term related to $\bar{\delta}^c$ in (2.81) is present or absent depending on the motion being unsteady or steady, while in the incompressible case the transpiration velocity is not affected by unsteady effects.

3. Numerical procedures

The Fourier coefficients $\{\hat{u}_{m,n},\ \hat{v}_{m,n},\ \hat{w}_{m,n},\ \hat{\tau}_{m,n},\ \hat{p}_{m,n}\}$ are obtained by solving the boundary-region equations (2.23)–(2.27) with the initial conditions (2.78) and the boundary conditions (2.80). The wall-normal domain extends to $\eta_{max} = 60$ and 2000 grid points are used in this direction. The typical step size in the marching direction is $\Delta\bar{x} = 10^{-3}$. The resulting block tri-diagonal system is solved using a standard block elimination algorithm. In order to avoid the pressure decoupling phenomenon, the pressure is computed on a grid that is staggered in the η direction with respect to the grid for the velocity and temperature. The nonlinear terms are evaluated using the pseudo-spectral method (Canuto *et al.* 1988). Dealiasing is performed by following the so-called 3/2-rule, which prevents the spurious cascade from the unresolved higher-frequency modes into the resolved low-frequency modes (Canuto *et al.* 1988).

The density fluctuations are calculated using (2.19), where the first term is neglected with respect to the other two because $k_x/R_\lambda \ll 1$. The viscosity fluctuations are evaluated using (2.21) and by excluding the mean flow and the linear part of the disturbance from (2.21). The following steps are performed to obtain $\hat{\rho}_{m,n}$ and $\hat{\mu}_{m,n}$.

(1) The temperature fluctuation $\hat{\tau}_{m,n}$ is transformed from the spectral to the physical space to calculate $\bar{\tau}$.

(2) The fluctuations of density and viscosity are evaluated as follows

$$\bar{\rho} = -\frac{\bar{\tau}}{T(T + r_t\bar{\tau})}, \quad \bar{\mu} = \sum_{j=2}^{\infty} \frac{(\omega_j)}{j!} T^{\omega-j} r_t^{j-2} \bar{\tau}^j. \tag{3.1a,b}$$

(3) The latter are transformed back to the spectral space to obtain $\hat{\rho}_{m,n}$ and $\hat{\mu}_{m,n}$.

A second-order predictor–corrector scheme is used to calculate the nonlinear terms while marching downstream. Extensive resolution checks have been carried out to verify the accuracy of the code. The amplitudes of the truncated Fourier series are six or seven orders of magnitude smaller than that of the forcing modes and so they do not significantly affect the flow dynamics. Use of $N_t = N_z = 9$ is sufficient to capture the nonlinear effects in the case $r_t = 2$, while for $r_t = 4$ an accuracy of the same order is obtained with $N_t = N_z = 13$.

To calculate the outer-flow field in the subsonic case, we solve the Helmholtz equation (2.41) numerically with $M_\infty < 1$ to obtain $\hat{\Phi}_m(\bar{x},\ \bar{y})$, and the Fourier coefficients $\hat{\phi}_m(\bar{x},\ \bar{y})$ are then retrieved from (2.40). The computational domain for $\bar{x} \geqslant 0$ extends sufficiently downstream for the forcing at $\bar{y} = 0$ to vanish. The symmetry about $\bar{y} = 0$ implies that the homogeneous Neumann boundary condition $\partial\hat{\Phi}_m/\partial\bar{y} = 0$ is used at $\bar{y} = 0$ and $\bar{x} < 0$. Careful resolution checks have been performed to ensure that the solution is independent of the size of the computational domain. The Helmholtz equation is discretized with a second-order finite difference scheme in $\bar{x}$ and $\bar{y}$. The resulting block tri-diagonal matrix is solved at each point using the generalized minimum residual method (Saad & Schultz 1986) with diagonal preconditioner implemented in the iterative methods library, IML++ (Dongarra *et al.* 2006).

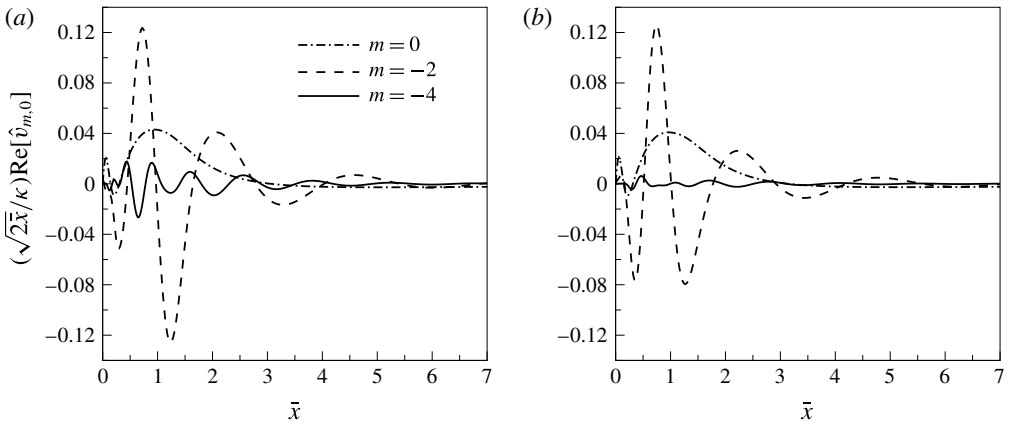

FIGURE 2. Large-η limit of $\hat{v}_{m,0}$ for $M_\infty = 0.69$ (a) and $M_\infty = 3$ (b).

4. Results for the outer flow

The solution for the irrotational part of the outer flow $\bar{\boldsymbol{q}}_0(\bar{x}, \bar{y}, \bar{t})$ (refer to (2.28)) is studied in this section. The streamwise and wall-normal velocity components, $\bar{u}_0(\bar{x}, \bar{y}, \bar{t})$ and $\bar{v}_0(\bar{x}, \bar{y}, \bar{t})$, are calculated for two different flow regimes: a subsonic case with $\{M_\infty, R_\lambda, r_t, \kappa\} = \{0.69, 600, 3.6, 1.3\}$ and a supersonic case with $\{M_\infty, R_\lambda, r_t, \kappa\} = \{3, 1000, 3.6, 1.12\}$.

The displacement-induced transverse velocity $\hat{v}_{m,0}$ given in (2.82) represents, after multiplication by $\sqrt{2\bar{x}}/\kappa$, the Neumann boundary condition at $\bar{y} = 0$ for $\hat{\phi}_m$ and is shown for the subsonic and supersonic cases in figure 2. Only the real part of the modes with $|m| = 0,\ 2,\ 4$ is considered, as the imaginary part is similar to the real part and higher harmonics are negligible. Physically, the terms $\hat{v}_{m,0}(\bar{x},\ \eta \gg 1)$ represent the harmonics of a spanwise-averaged time-periodic modulation which is superimposed onto the slope of the Blasius displacement thickness. In the light of the thin airfoil theory analogy, this modulation is interpreted as the strength of the pulse source distribution.

In the subsonic case, due to the difficulty in calculating the integral in (2.47), the solution is obtained numerically, as explained in § 3. In the supersonic case, the solution (2.46) is employed to calculate the Fourier coefficients $\hat{\phi}_m(\bar{x}, \bar{y})$, from which $\bar{u}_0(\bar{x}, \bar{y}, \bar{t})$ and $\bar{v}_0(\bar{x}, \bar{y}, \bar{t})$ are obtained. The pressure $\bar{p}_0(\bar{x}, \bar{y}, \bar{t})$ is derived from (2.50).

Contours of $\bar{u}_0$, $\bar{v}_0$ and $\bar{p}_0$ in the $\bar{x}$–$\bar{y}$ plane, which represent the acoustic field emitted by streaks, are shown in figures 3 and 4 at two different times $\bar{t}$ for the subsonic and supersonic cases, respectively. According to (2.56) the temperature $\bar{\tau}_0$ differs from $\bar{p}_0$ by a factor $(\gamma - 1)M_\infty^2$, which is equal to 0.19 and 3.6 in the two flow regimes. The scale for the temperature $\bar{\tau}_0$ is thus reported together with that for the pressure.

In the subsonic case, the influence of the boundary-layer thickness pulsation propagates in all directions from the plate and gradually diminishes as the distance from the body increases. The streamwise modulation of the solution is caused by the oscillatory forcing at $\bar{y} = 0$, which corresponds to a sequence of sources with positive and negative strength (refer to figure 2). The apparent 'wavelength' of modulation is $\Delta\bar{x} \approx 0.5$. The outer-flow solution shows the most intense peaks for $0.5 < \bar{x} < 2$, i.e. where the forcing is strongest.

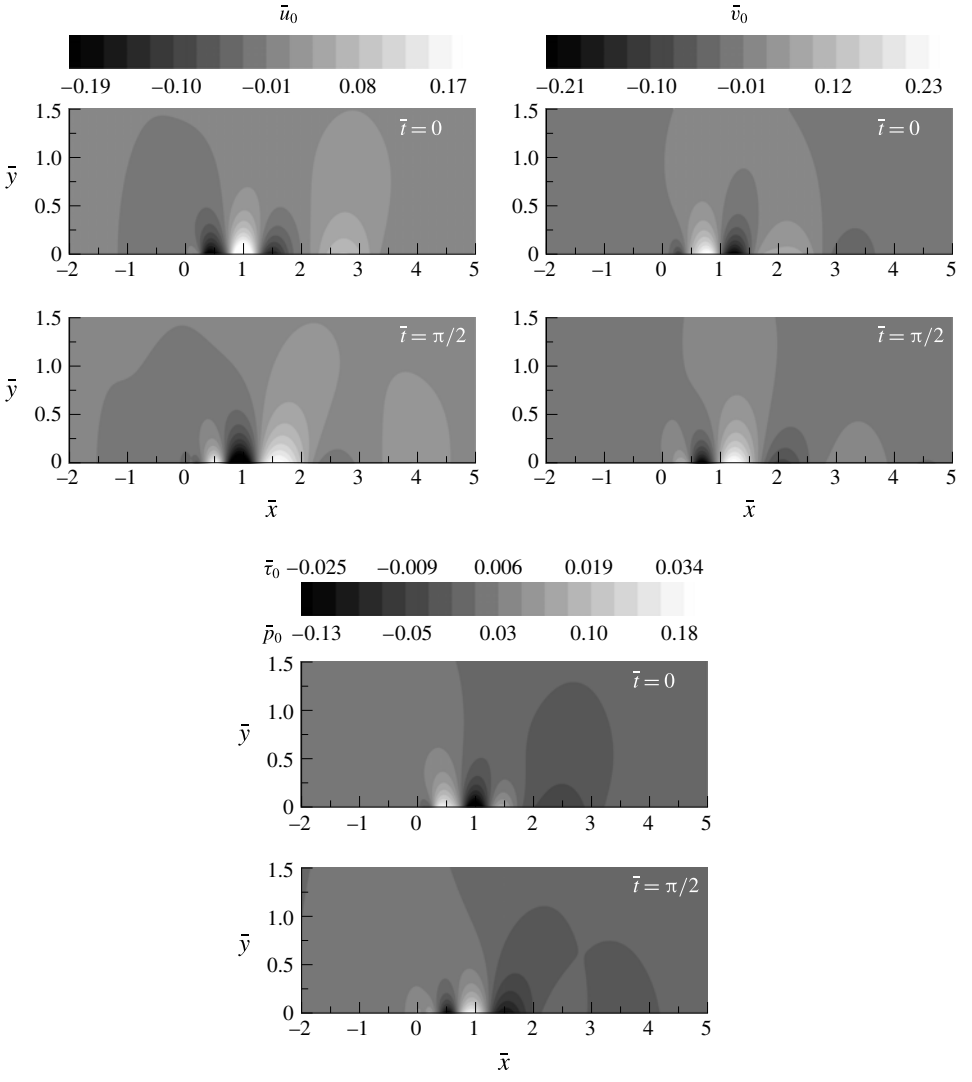

FIGURE 3. Contours of the streamwise and wall-normal velocity components, $\bar{u}_0$ and $\bar{v}_0$, the pressure $\bar{p}_0$ and the temperature $\bar{\tau}_0$ in $\bar{x}$–$\bar{y}$ plane, at different times $\bar{t}$ for $M_\infty = 0.69$.

The supersonic solution, shown in figure 4, is non-zero only inside the Mach dihedron delimited by the Mach line $\bar{y} = \bar{x}/\sqrt{M_\infty^2 - 1}$, as in the thin airfoil theory (Dragos 2004, p. 32). The magnitude of the disturbance is constant along the Mach line and thus the perturbations do not vanish as $\bar{y} \to \infty$.

5. Results for the boundary-layer streaks

The parameters for the numerical results are selected to be representative of two possible applications: subsonic turbomachinery and supersonic flight conditions. The former is characterized by a relatively low Mach number and an intense turbulence

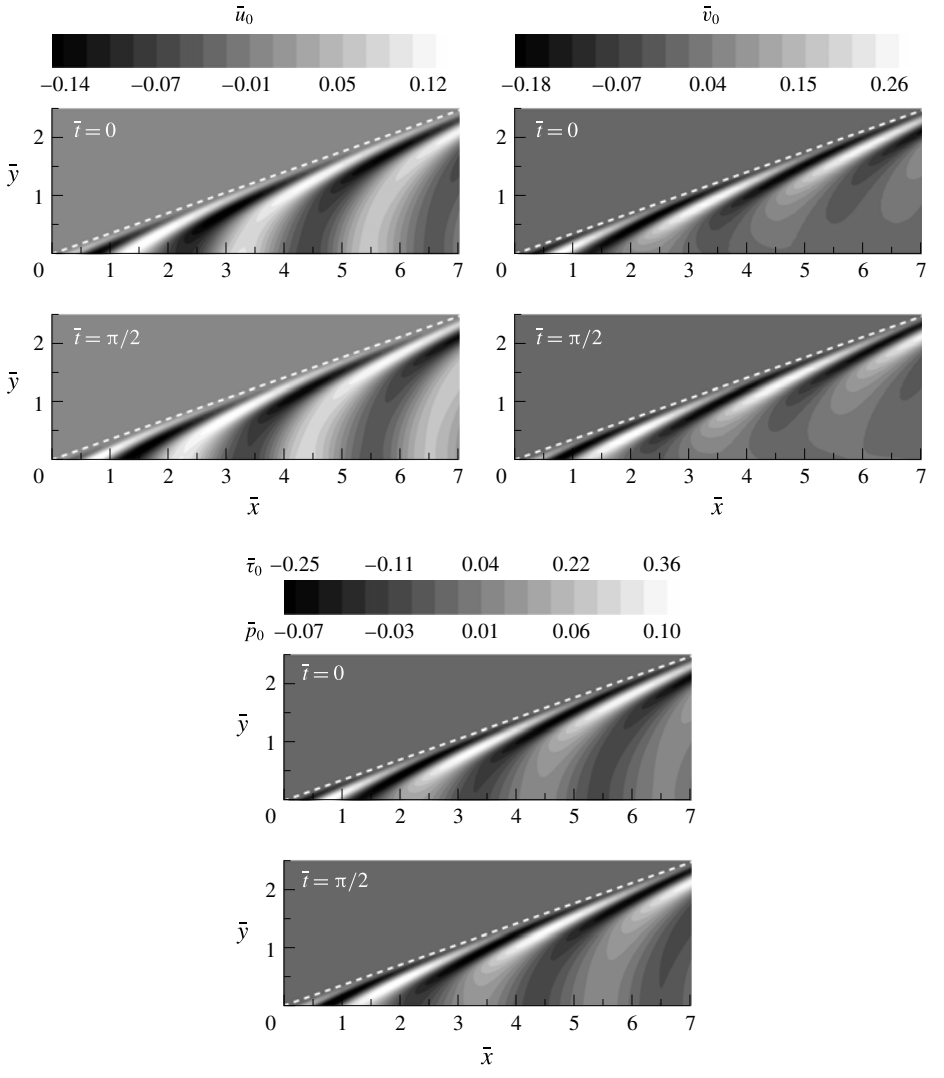

FIGURE 4. Contours of the streamwise and wall-normal velocity components, $\bar{u}_0$ and $\bar{v}_0$, the pressure $\bar{p}_0$ and the temperature $\bar{\tau}_0$ in the $\bar{x}$–$\bar{y}$ plane, at different times $\bar{t}$ for $M_\infty = 3$. The dashed lines represent the Mach line $\bar{y} = \bar{x}/\sqrt{M_\infty^2 - 1}$.

level, while the latter features a higher Mach number and a quieter disturbance environment. An idealized case of a supersonic wind tunnel flow with no acoustic modes is also considered. In all the cases, the scaled amplitudes of the free-stream turbulence velocity components are: $\hat{u}^\infty_{x,\pm} = \hat{u}^\infty_{y,\pm} = 1$ and $\hat{u}^\infty_{z,\pm} = \mp 1$. Through continuity (2.4), this leads to the following relation for the wavenumbers: $k_x + k_y - 1 = 0$.

In the following, the parameters employed for the three sets of calculations are presented and the relevant results are shown. The reader may skip § 5.1 without loss of clarity.

5.1. *Choice of parameters*

5.1.1. *Turbomachinery applications*

With a reference to typical experimental works on turbomachinery applications (e.g. Camci & Arts 1990) the following parameters are adopted: unit Reynolds number $R^*_{1\infty} = U^*_\infty/\nu^*_\infty = 8 \times 10^6$ m^{-1}, chord length $\ell^* = 8$ cm, free-stream temperature $T^*_\infty = 500$ K and kinematic viscosity of air $\nu^*_\infty = 3.9 \times 10^{-5}$ m^2 s^{-1}, free-stream Mach number $M_\infty = 0.69$ and turbulence level $Tu = 0.8 - 5.2\,\%$. Although we have chosen our flow parameters to be as close as possible to the experimental ones, important extra factors are present in real experimental and technological flow systems, such as acoustic free-stream forcing, surface curvature, pressure gradient and wall cooling. These can be taken into account by suitable extensions of the present framework. For example, the boundary-region equation approach has been extended to study the generation and development of Görtler vortices in the incompressible boundary layer over a concave wall (Wu, Zhao & Luo 2011). With further progress, precise quantitative comparisons with experiments and applications to practical situations would be possible. Presently, the results are of qualitative value as far as their relevance to turbomachinery is concerned. The adiabatic wall temperature is calculated using the following relation valid for a perfect gas,

$$T^*_{ad} = T^*_\infty \left(1 + C_t \frac{\gamma - 1}{2} M^2_\infty\right), \tag{5.1}$$

where $C_t = \sqrt{Pr}$ is the recovery factor for a laminar boundary layer over a flat plate. The resulting adiabatic wall temperature, $T^*_{ad} = 540.5$ K, is in the range of typical turbine rotor applications. The ratio of the wall temperature to the adiabatic wall temperature $T^*_w/T^*_{ad} = 0.7$ is chosen to mimic realistic aero-engine conditions (Zhang & He 2014), where blade cooling is most often applied to avoid excessive surface temperature. The resulting non-dimensional wall temperature is $T_w = 0.75$.

As the relevant length scales and spectra of the free-stream turbulence are not documented in the experiments, we choose to assume that the ratio of the streamwise integral scale to the chord is equal to 1.5. It follows that $\lambda^*_x = 0.12$ m and the frequency $f^* = U^*_\infty/\lambda^*_x = 2.5$ kHz. At downstream locations where $x^* = O(\lambda^* R_\lambda)$, the boundary-layer thickness is comparable with the spanwise length scale λ^*. The laminar boundary-layer thickness is proportional to $\sqrt{\nu^*_\infty x^*/U^*_\infty}$, and it is estimated that transition occurs at $x^*_T/\ell^* = 0.67$ (i.e. $x^*_T = 5.36$ cm), which corresponds to a critical Reynolds number of 5×10^5 (Schlichting & Gersten 2000). It follows that the boundary-layer thickness δ^*_{99}, defined as the wall-normal location where $U = 0.99$, is 0.41 mm, and the displacement thickness is $\delta^* = 0.14$ mm. The latter value is taken as the reference length scale λ^*. The Reynolds number R_λ and the scaled streamwise wavenumber κ are worked out by use of (2.5) and (2.7). The free-stream disturbance intensity is defined as $Tu = 2\epsilon\sqrt{(\hat{u}^\infty_{x,+})^2 + (\hat{u}^\infty_{x,-})^2}$. For our choice of $\hat{u}^\infty_{x,\pm} = 1$, $Tu = 2\sqrt{2}\epsilon$. Given ϵ and R_λ, the turbulence Reynolds number r_t is calculated from (2.8). The influence of nonlinear effects is investigated by varying the turbulence level (i.e. ϵ) with all the other parameters kept constant, as shown in table 1(a). Two different values of $\lambda^*_x/\ell^* = 0.77$, 3.1 are considered in order to study the effect of the streamwise wavenumber (refer to table 1(b)). The relation between λ^*_z, shown in table 1, and λ^* is $\lambda^*_z = 2\pi\lambda^*$.

	U^*_∞ (m s^{-1})	ν^*_∞ (m^2 s^{-1}) ($\times 10^4$)	T^*_∞ (K)	λ^*_z (m) ($\times 10^3$)	λ^*_x (m)	δ^*_{99} (m) ($\times 10^3$)	f^* (kHz)	M_∞	R_λ	k_x ($\times 10^3$)	κ	Tu (%)	r_t
						Turbomachinery							
(a)	309	0.39	500	0.89	0.12	0.41	2.5	0.69	1 124	7.3	0.35	0.7	2.7
	309	0.39	500	0.89	0.12	0.41	2.5	0.69	1 124	7.3	0.35	2	7.9
(b)	309	0.39	500	0.89	0.25	0.41	1.25	0.69	1 124	3.6	0.5	1.3	5.3
	309	0.39	500	0.89	0.06	0.41	5	0.69	1 124	14.2	0.25	1.3	5.3
						Flight							
(c)	592	2.67	218	9.4	2.5	2.6	0.24	2	3 343	3.85	0.28	0.41	4.8
	1776	2.67	218	9.4	7.4	3.8	0.24	6	10 029	1.28	0.28	0.14	4.8
(d)	888	2.67	218	9.4	3.68	2.8	0.24	3	5 014	2.6	0.28	0.19	3.37
	888	2.67	218	9.4	3.68	2.8	0.24	3	5 014	2.6	0.28	0.35	6.25
						Wind tunnel							
(e)	646	0.37	115.4	2	1.3	1.2	0.5	3	5 400	1.55	0.34	0.11	2.1
	646	0.37	115.4	2	1.3	1.2	0.5	3	5 400	1.55	0.34	0.23	4.4
	646	0.37	115.4	2	1.3	1.2	0.5	3	5 400	1.55	0.34	0.31	6

TABLE 1. Choice of the parameters for the turbomachinery, flight and wind tunnel cases.

5.1.2. *Flight conditions*

The data reported in Schneider (1999) are analysed to infer typical parameters for supersonic flight conditions. The following values are adopted: free-stream Mach number $M_\infty = 3$, unit Reynolds number $R^*_{1\infty} = 3.33 \times 10^6$ m^{-1} and wall temperature ratio $T^*_w/T^*_{ad} = 0.5$. The latter value is in the typical range of high supersonic flight speeds, where, in addition to aerodynamic heating, radiative cooling also occurs due to the solid wall of the body radiating energy from the surface (Fedorov & Khokhlov 2001). A free-stream temperature $T^*_\infty = 218$ K is assumed at a typical altitude for supersonic flight of 20 km (Wilson, Love & Larson 1971). It follows that the velocity and the kinematic viscosity of air in the free stream are $U^*_\infty = 888$ ms^{-1} and $\nu^*_\infty = 2.67 \times 10^{-4}$ m^2 s^{-1}. From (5.1) the adiabatic wall temperature $T^*_{ad} = 548$ K is obtained. It follows that $T^*_w = 274$ K. The boundary-layer thickness δ^* at high Mach number is assumed to grow as $x^* M^2_\infty/\sqrt{R_x}$, where R_x is the local Reynolds number at the edge of the boundary layer (refer to Anderson 2006, equation (7.9)). At the transition-onset location $x^*_T = 0.1$ m (Schneider 1999) and $\delta^* = 1.5$ mm, which is taken as the reference length scale, i.e. $\lambda^* = \delta^*$.

Considering the data reported in figure 6 of Wilson *et al.* (1971) and figure 1 of Hocking (1985) on the atmospheric turbulence power spectra and scales, a streamwise wavelength $\lambda^*_x = 3.68$ m is chosen. The corresponding frequency is $f^* = 240.8$ Hz. In-flight measurements by Riedel & Sitzmann (1998) and Saric (2008) indicate that the turbulence level in subsonic flight for the quiescent air atmosphere is 0.05 %–0.06 %. For the high-altitude environment of a supersonic aircraft, Coleman & Steiner (1960) and Ehernberger & Love (1975) report even lower turbulence intensities. However, close to inversion layers (i.e. areas where the usual trend of decrease in air temperature with increasing altitude is reversed) or within clouds, large turbulence levels in the range $0.1\,\% < Tu < 1\,\%$ or more may occur (Zanin 1985). The turbulence levels for our simulations are chosen as representative of these atmospheric conditions ($0.1\,\% < Tu < 0.3\,\%$).

The influence of compressibility is investigated by varying M_∞. It is assumed that the variation of M_∞ is only due to a variation of the free-stream velocity U^*_∞, while the free-stream temperature T^*_∞ is unchanged. Therefore, a^*_∞ and ν^*_∞ are also constant. The wall temperature is the same in all the cases, while T^*_{ad} varies according to (5.1) for different Mach numbers. The dimensional amplitude of the gust is kept fixed at 2.39 m s^{-1}. It follows that the turbulence level decreases as the free-stream velocity increases, but the turbulence Reynolds number, which is defined by (2.8), does not change because R_λ increases linearly with U^*_∞. The dimensional frequency is kept constant and it corresponds to different λ^*_x depending on U^*_∞, as presented in table 1(c). In order to analyse the effect of nonlinearity at supersonic speeds, two different turbulence levels, $Tu = 0.19\,\%$ and $0.35\,\%$, are considered for $M_\infty = 3$ (refer to table 1(d)).

5.1.3. *Wind tunnel conditions*

The following parameters are chosen as representative of typical supersonic wind tunnel experiments (Beckwith & Miller 1990; Graziosi & Brown 2002; Fedorov *et al.* 2003): $M_\infty = 3$, $U^*_\infty = 646$ m s^{-1}, $\nu^*_\infty = 3.7 \times 10^{-5}$ m^2 s^{-1}, $T^*_\infty = 115.4$ K, $f^* = 500$ Hz, $k_x = 1.55 \times 10^{-3}$, $R_\lambda = 5400$ and $\kappa = 0.34$. The calculations are performed for three different turbulence levels, $Tu = 0.11\,\%$, $0.23\,\%$, $0.31\,\%$, which correspond to $r_t = 2.1$, 4.4, 6 (refer to table 1(e)). The representation is idealized since acoustic disturbances are excluded.

For these cases the ratio between the wall temperature and the adiabatic wall temperature provided by Graziosi & Brown (2002), $T^*_w/T^*_{ad} = 1.1$, is employed. The results for this hot-wall condition will be compared with those obtained with the adiabatic condition $T^*_w = T^*_{ad}$ and with the cold-wall condition employed by Fedorov *et al.* (2003), where $T^*_w/T^*_{ad} = 0.8$.

5.2. *Evolution of nonlinear compressible streaks*

As anticipated on the basis of the linear analysis by Ricco & Wu (2007), free-stream disturbances of the hydrodynamic kind (i.e. convected gusts) generate thermal fluctuations inside the boundary layer due to the velocity–temperature coupling. Just as the temperature profile affects the stability of a two-dimensional flow (Lees 1947; Mack 1975), thermal streaks are bound to influence the secondary instability of the streaky boundary layer. We will therefore focus on the fluctuations of the streamwise velocity and temperature inside the boundary layer.

The overall intensity of the streak signature, which comprises all the harmonics in the nonlinear regime, is measured by the root-mean-square (r.m.s. hereinafter) of the fluctuating quantity, defined as

$$q_{rms} \equiv r_t \sqrt{\sum_{m=-\bar{N}_t}^{\bar{N}_t} \sum_{n=-\bar{N}_z}^{\bar{N}_z} |\hat{q}_{m,n}|^2}, \quad m \neq 0, \tag{5.2}$$

where q may stand for the streamwise velocity or the temperature and $\bar{N}_t = (N_t - 1)/2$, $\bar{N}_z = (N_z - 1)/2$. The downstream development of the maximum q_{rms} along η,

$$q_{rms,max}(\bar{x}) = \max_\eta q_{rms}(\bar{x}, \eta), \tag{5.3}$$

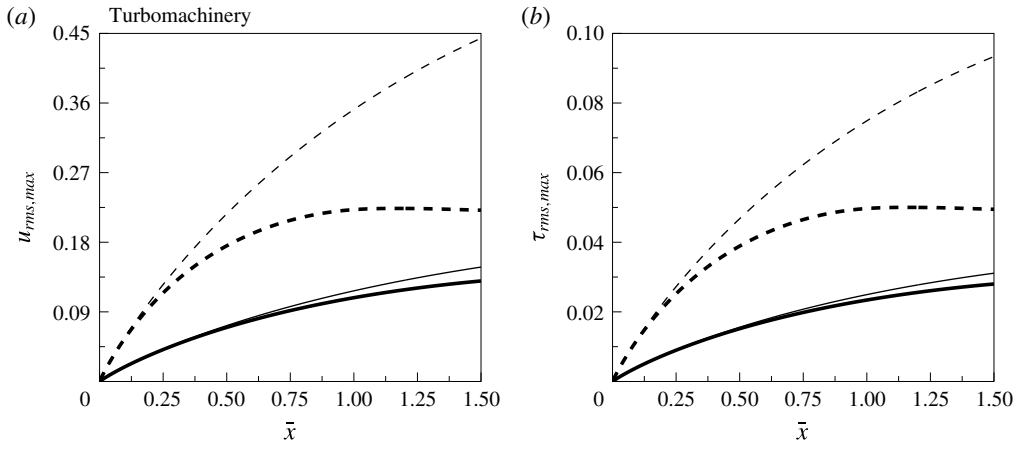

FIGURE 5. Evolution of the maximum r.m.s. of the streamwise velocity (*a*) and the temperature (*b*) for different values of the turbulence Reynolds number: $r_t = 2.7$ (solid lines), $r_t = 7.9$ (dashed lines) at $M_\infty = 0.69$ (refer to table 1(a)). Thick lines: nonlinear solutions, thin lines: linearized solution.

is shown in figures 5 (turbomachinery case), 6 (flight case) and 7 (wind tunnel case), where the nonlinear solutions are compared with the corresponding linearized approximations for different values of *Tu*. In the linear case, the peak of the r.m.s. is given by

$$q_{rms,max} = \epsilon\sqrt{2}(k_z/k_x)\sqrt{|u_{z,w,+}|^2 + |u_{z,w,-}|^2}\max_{\eta}|\bar{q}_l(\bar{x},\,\eta)|, \tag{5.4}$$

where $\bar{q}_l$ represents the solution provided by Ricco & Wu (2007). Since $|u_{z,w,+}| = |u_{z,w,-}| = |u_{z,w}|$, (5.4) simplifies to:

$$q_{rms,max} = 2\epsilon(k_z/k_x)|u_{z,w}|\max_{\eta}|\bar{q}_l(\bar{x},\,\eta)|. \tag{5.5}$$

Sufficiently upstream, the linear and nonlinear solutions overlap as the influence of nonlinearity is still weak. Due to the continued amplification of the disturbance, the streak signature becomes stronger and the linear and nonlinear solutions start diverging for moderate r_t. In the case with the lowest r_t for all the three scenarios considered, the linear and nonlinear curves are almost indistinguishable. In the cases with higher r_t, a stabilizing effect of nonlinearity is observed on the streamwise velocity and temperature and, as the turbulence intensity increases, the attenuation of the disturbances is enhanced. The higher the turbulence level, the slower and the weaker the disturbance growth becomes, and the farther upstream the nonlinear effects start asserting their influence. The stabilizing effect of nonlinearity was already observed by Ricco *et al.* (2011) in the incompressible regime for high turbulence levels. Here, it is shown that nonlinear effects play the same role on thermal (temperature) streaks.

For the turbomachinery case (figure 5), the attenuation of the streaks is more pronounced than in flight conditions as the turbulence levels are higher, and the deviation of the kinematic and thermal streaks from the linearized solution is of similar magnitude. The kinematic fluctuations are approximately one order of

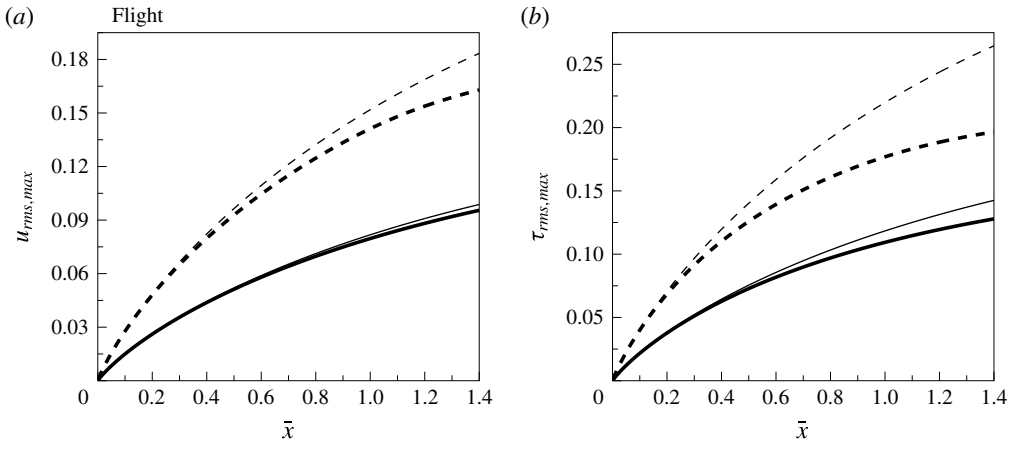

FIGURE 6. Evolution of the maximum r.m.s. of the streamwise velocity (*a*) and the temperature (*b*) for different values of the turbulence Reynolds number: $r_t = 3.37$ (solid line), $r_t = 6.25$ (dashed lines) at $M_\infty = 3$ (refer to table 1(d)). Thick lines: nonlinear solutions, thin lines: linearized solutions.

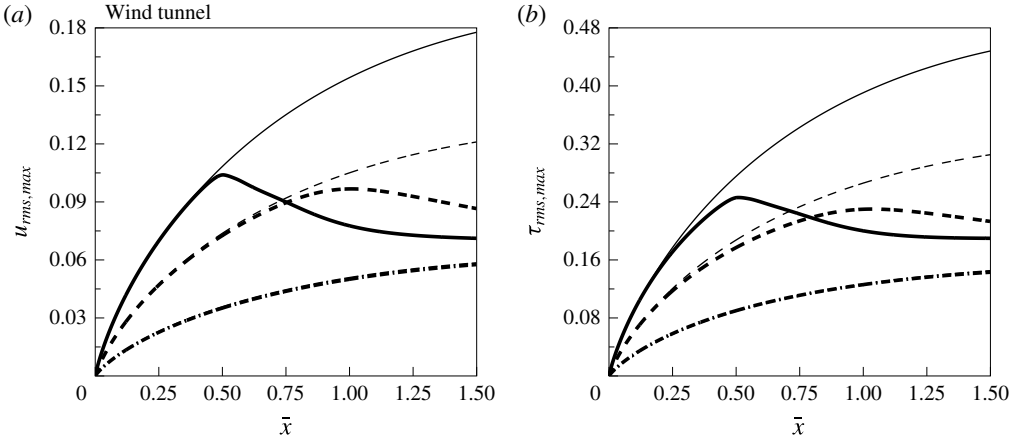

FIGURE 7. Evolution of the maximum r.m.s. of the streamwise velocity (*a*) and temperature (*b*) for different values of the turbulence Reynolds number: $r_t = 2.1$ (dashed-dotted lines), $r_t = 4.4$ (dashed lines), $r_t = 6$ (solid lines) at $M_\infty = 3$ (refer to table 1(e)). Thick lines: nonlinear solutions, thin lines: linearized solutions.

magnitude higher than the thermal streaks relatively to the correspondent free-stream mean velocity and temperature.

In flight conditions (figure 6), because of a higher Mach number, the temperature fluctuation acquires a large intensity, which is comparable with that of the velocity fluctuation. Although the influence of *Tu* on the streamwise velocity is quite weak even in the highest turbulence intensity case, $r_t = 6.25$, appreciable attenuation of the nonlinear thermal streaks with respect to the linearized ones is observed. The stabilizing effect is more marked on the temperature than on the streamwise velocity. The nonlinear and linear r.m.s. of the temperature streaks diverge farther upstream than the r.m.s. of the streamwise velocity. Even for a low-disturbance environment such

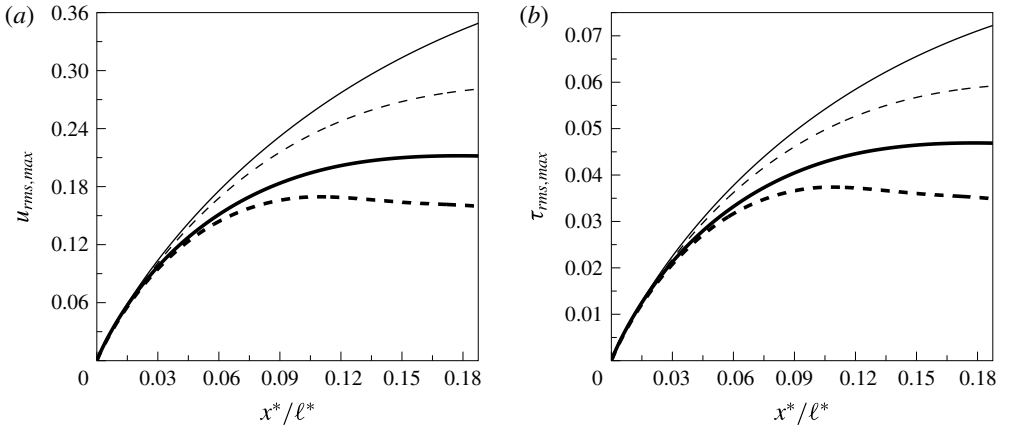

FIGURE 8. Evolution of the maximum r.m.s. of the streamwise velocity (*a*) and the temperature (*b*) for different streamwise wavenumber: $k_x = 0.0036$ (solid lines) and $k_x = 0.0142$ (dashed lines) at $M_\infty = 0.69$ (refer to table 1(b)). Thick lines: nonlinear solutions, thin lines: linearized solutions.

as free flight, it seems necessary to describe the formation and amplification of the streaks correctly by taking into account the nonlinear interactions inside the boundary layer.

In the wind tunnel case shown in figure 7, a peculiar behaviour of the nonlinear curve for the highest turbulence level case is observed. A sharp deviation of the nonlinear solution from the linear one occurs at $\bar{x} \approx 0.5$, which corresponds to a physical downstream position of $x^* \approx 10$ cm. This phenomenon was not observed in the incompressible cases studied by Ricco *et al.* (2011). The parameters used in this case are very similar to those of the flight case with highest r_t (refer to tables 1(d) and 1(e)), except that k_x is approximately half of that in the flight case. As a consequence, the effect of nonlinearity is stronger. The streamwise wavenumber of the wind tunnel case is comparable with that of the flight case with $M_\infty = 6$ (refer to table 1(c)) but r_t is smaller and M_∞ is higher in the latter, thus resulting in weaker nonlinear effects. Additional calculations suggest that this abrupt change occurs when a sufficiently small streamwise wavenumber is employed, i.e. $k_x \leqslant 1.5 \times 10^{-3}$, together with a high turbulence Reynolds number, $r_t \geqslant 6$, at supersonic speed. In the subsonic regime no such sharp deviation was observed, even at high r_t.

The effect of the frequency is displayed in figure 8, where the downstream evolutions of $u_{rms,max}$ and $\tau_{rms,max}$ are plotted for different values of k_x in the turbomachinery case (refer to table 1(b)). The fluctuations of the streamwise velocity and temperature are higher for smaller k_x, but the dependence of the stabilizing effect of nonlinearity on the frequency is very weak and it is the same for the streamwise velocity component and the temperature. For $k_x \geqslant 0.01$ the amplitude saturates at an almost constant value before decaying farther downstream.

Figure 9 displays the signature of the streamwise velocity and temperature for different Mach numbers in the flight case (refer to table 1(c)). The variation of M_∞ is only due to a variation of U^*_∞, while T^*_∞ is constant. As the Mach number increases the r.m.s. of the streamwise velocity is attenuated while the temperature fluctuations are intensified. For $M_\infty = 6$, the latter acquire an intensity as large as 26 % of T^*_∞, whereas the velocity fluctuations merely reach 5 % of U^*_∞. The result suggests

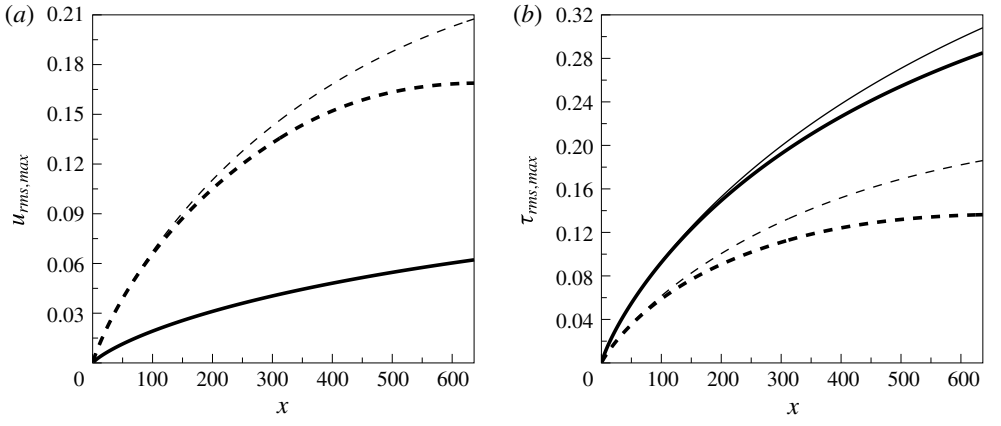

FIGURE 9. Evolution of the maximum r.m.s. of the streamwise velocity (*a*) and the temperature (*b*) for different free-stream Mach numbers: $M_\infty = 2$ (dashed lines), $M_\infty = 6$ (solid lines). The turbulence Reynolds number is $r_t = 4.8$ (refer to table 1(c)). Thick lines: nonlinear solutions, thin lines: linearized solutions.

that thermal streaks are likely to be the primary cause of secondary instability in high speed flows. Figure 9 also shows that the attenuation effect on the velocity is stronger than the enhancement of the temperature. For example, tripling the Mach number from 2 to 6 results in a decrease of more than three times in the r.m.s. of the streamwise velocity and an increase of twice in the temperature signature at $x = 600$. Despite r_t being the same, for higher M_∞ the stabilizing effect of nonlinearity becomes less pronounced and this is more evident for the streamwise velocity r.m.s., whose nonlinear evolution is indistinguishable from the linearized curve in the highest M_∞ case. This behaviour is attributed to the turbulence level being smaller for higher values of the free-stream velocity, although r_t is the same in all the cases.

In figure 10 the results obtained in the wind tunnel case with $r_t = 6$ for the hot-wall condition $T^*_w/T^*_{ad} = 1.1$ are compared with those relative to a cold-wall condition $T^*_w/T^*_{ad} = 0.8$ and an adiabatic temperature at the wall $T^*_w = T^*_{ad}$. As the wall heat flux increases from negative (heating), to zero (adiabatic) and to positive (cooling), the signature of the streamwise velocity is enhanced while the temperature disturbance is attenuated. The position where the abrupt deviation occurs moves from $\bar{x} \approx 0.5$ in the hot-wall case to $\bar{x} \approx 0.7$ in the cold-wall case. Therefore the wall heat flux influences the position where the onset of the stabilizing effect due to nonlinearity occurs. This suggests that the employment of the adiabatic wall condition in wind tunnel experiments may lead to an inaccurate prediction of the transition location for high Mach number supersonic flight conditions, where wall cooling usually needs to be employed for thermal protection.

5.3. *Wall-normal profiles of the perturbation for flight condition*

The wall-normal profiles of the streamwise velocity and the temperature are now examined for flight conditions with $M_\infty = 3$ and $r_t = 4.8$, as this case features significant effects of nonlinearity and compressibility, whereas in the turbomachinery case compressible effects are weak. The parameters correspond to case (d) in table 1, except that $Tu = 0.27\,\%$ and $r_t = 4.8$. The flow is symmetric with respect to the z direction because the Fourier forcing modes have opposite spanwise wavenumbers

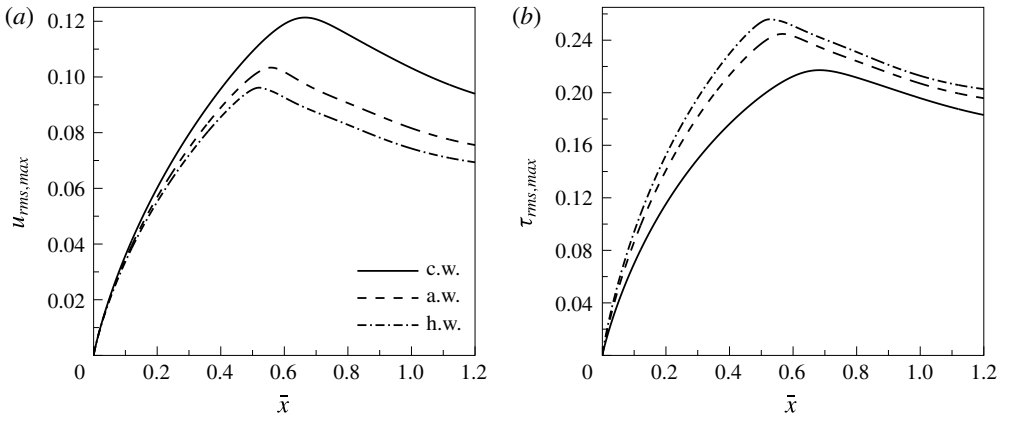

FIGURE 10. Evolution of the maximum r.m.s. of the streamwise velocity (*a*) and the temperature (*b*) for different wall temperature conditions: hot wall (h.w.), adiabatic wall (a.w.) and cold wall (c.w.) at $M_\infty = 3$.

but equal amplitude. Therefore, results will only be presented for modes with $n \geqslant 0$, since modes (m, n) and $(m, -n)$ have the same amplitude and shape.

Figure 11 shows the profiles of the spanwise-uniform time-averaged flow distortion $(0, 0)$, the forcing mode $(-1, 1)$, and the second and third harmonics with $|m| = |n|$, i.e. $(-2, 2)$ and $(-3, 3)$, at $\bar{x} = 0.5$ and 1.2. As expected, the forcing mode has a higher amplitude than the other components. The mean-flow distortion makes a significant contribution to the overall flow. The magnitude of the higher harmonics decreases so quickly that the third harmonic becomes almost negligible. The profiles of the temperature perturbation are similar to those of the streamwise velocity and evolve in a similar manner, but the amplitude of the thermal fluctuations is slightly higher than those of the streamwise velocity (relatively to the free-stream values).

The streamwise velocity and temperature of the seeded modes attain their respective maxima at $\eta = 1.5$ and $\eta = 2$. The most pronounced peak of the second harmonic occurs at a larger wall-normal distance, $\eta = 3$. The mean-flow distortion of the streamwise velocity is positive near the wall and negative for $\eta > 2$, while the temperature profile (0, 0) is negative close to the plate (excluding a small positive region at $\eta < 0.5$) and positive in the outer layer. The (0, 0) components of the streamwise velocity and temperature grow significantly with the downstream distance and their amplitudes become greater than that of the seeded modes in the outer portion of the boundary layer, $\eta > 4$. The difference between the maximum values of the linear and nonlinear profiles is larger for the temperature than for the streamwise velocity. This confirms the stronger effect of nonlinearity on temperature for high-speed flows, which was already observed in figure 6. At $\bar{x} = 0.5$ the linear solution of $r_t|\hat{u}_{-1,1}|$ and $r_t|\hat{\tau}_{-1,1}|$ are almost indistinguishable from their nonlinear counterparts. At $\bar{x} = 1.2$ the peaks of $r_t|\hat{u}_{-1,1}|$ and $r_t|\hat{\tau}_{-1,1}|$ in the nonlinear case have moved closer to the wall and have decreased in comparison to the linear case. After reaching their maxima, the nonlinear solutions decay more slowly and become larger than the linearized approximations in the outer region of the boundary layer. The mean-flow distortion acquires an amplitude comparable with that of the seeded modes. Therefore, the effect of nonlinearity is to move the location of the disturbance peaks nearer to the

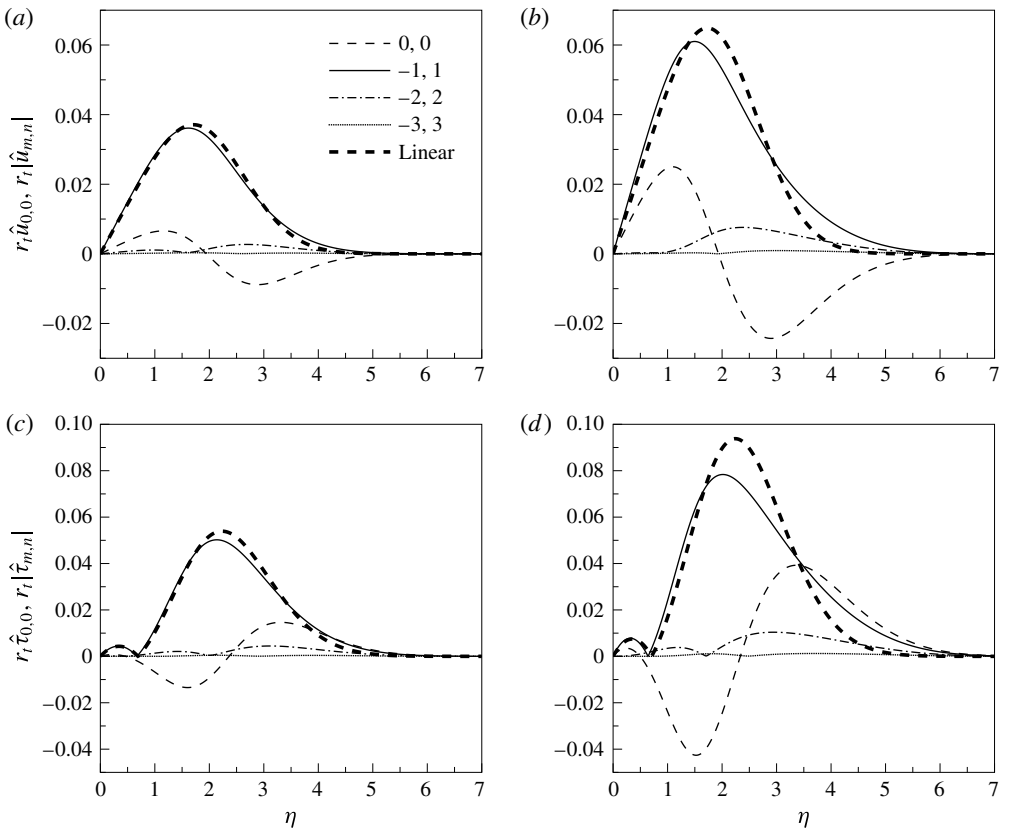

FIGURE 11. Profiles of the streamwise velocity (*a*,*b*) and the temperature (*c*,*d*) of the mean-flow distortion and harmonics with $|m| = |n| = 1, 2, 3$ at $\bar{x} = 0.5$ (*a*,*c*) and $\bar{x} = 1.2$ (*b*,*d*). The parameters correspond to the flight case with $M_\infty = 3$ and $r_t = 4.8$.

wall, to weaken the fluctuations in the core of the boundary layer while enhancing them close to the free stream, and most notably to generate significant mean-flow distortion.

As was pointed out by Ricco (2006), the nonlinear interactions generate only Fourier modes with $m = n$ when the flow is forced by a single free-stream mode, while in the case of a pair of oblique free-stream modes additional components with $m \neq n$ are induced. The nonlinearly generated modes are those with $|m| + |n|$ equal to an even integer, i.e. they are arranged as a checkerboard in spectral space. Those generated at the second and third orders are displayed in figure 12 at the downstream locations $\bar{x} = 0.5$ and 1.2. The amplitudes of the components $(-2, 0)$ and $(0, 2)$ are comparable with each other but approximately three times smaller than that of the mean-flow distortion $(0, 0)$. At $\bar{x} = 0.5$, the peak positions and the magnitudes of the modes $(-2, 0)$ and $(0, 2)$ are very similar (or almost identical for $\eta > 2$), while at $\bar{x} = 1.2$ the first peak of the mode $(-2, 0)$ becomes much higher than that of the component $(0, 2)$ and the second peak moves further from the wall. The third-order harmonics feature two or three humps, with the first or second peak being coincident with the valley of the second-order components. Profiles with three peaks were not observed in the incompressible case (Ricco *et al.* 2011) and they are more evident in the temperature streaks.

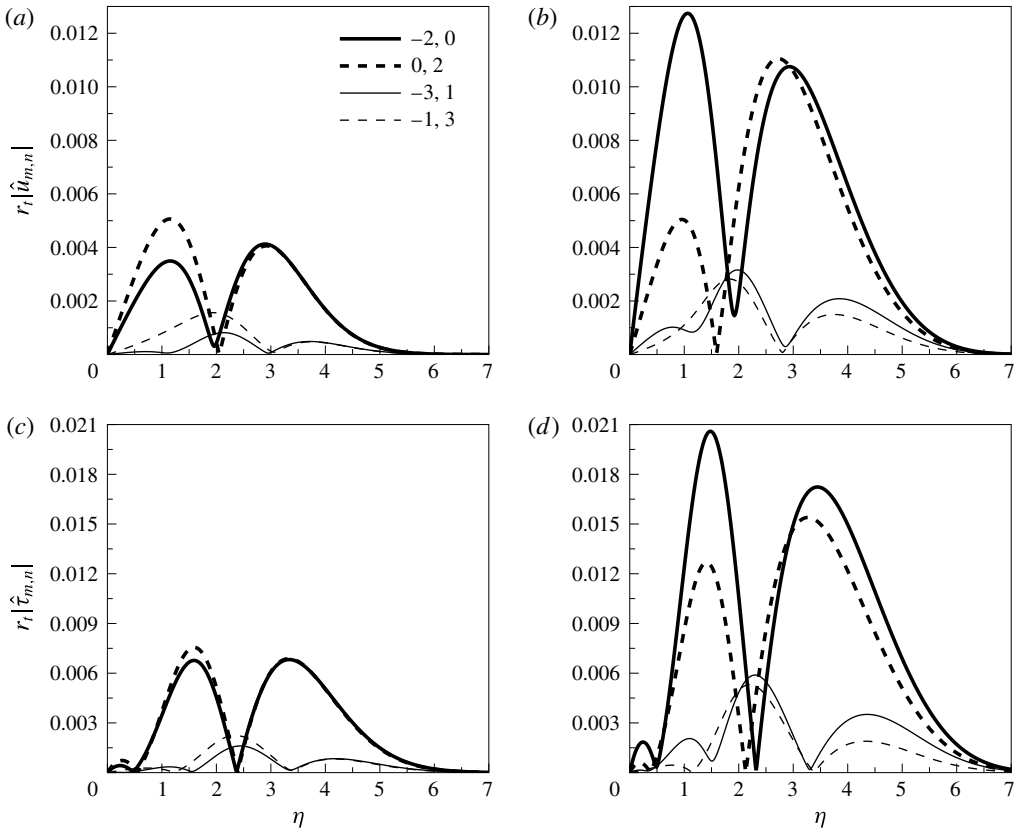

FIGURE 12. Profiles of the streamwise velocity (*a*,*b*) and the temperature (*c*,*d*) of harmonics with $m \neq n$ at $\bar{x} = 0.5$ (*a*,*c*) and $\bar{x} = 1.2$ (*b*,*d*). The parameters correspond to the flight case with $M_\infty = 3$ and $r_t = 4.8$.

The profiles of the cross-flow velocity components and of the pressure are displayed in figure 13. No mean spanwise velocity component is generated because the disturbances are symmetric with respect to the plane $z = 0$. The profiles of $\hat{v}_{m,0}$ asymptotically approach a constant value (with respect to η) in the free stream, as the right-hand side of (2.82) is a function of $\bar{x}$ only. The amplitudes of the wall-normal and spanwise velocity components are much smaller than that of the streamwise velocity, as $\sqrt{k_x/R_\lambda} = O(10^{-4})$ and $k_x/k_z = O(10^{-3})$.

The pressure fluctuations at the wall are analysed in order to show that these do not represent an aeroelasticity problem. The root-mean-square of the wall pressure is calculated and transformed in dimensional terms by multiplying it by $\rho^*_\infty U^{*2}_\infty$, where $U^*_\infty = 888$ m s^{-1} (table 1(d)) and $\rho^*_\infty = 0.09$ kg m^{-3} at 20 km altitude (Champion, Cole & Kantor 1985). The value obtained $p^*_{rms} = 0.055$ Pa is compared to the pressure difference on the wing. The latter is derived from the lift coefficient C_l, which is evaluated using the supersonic linearized theory (refer to Anderson 2007, equation (12.23)) and assuming an angle of attack equal to 10°. The resulting pressure difference $\Delta p^* = 4200$ Pa is five orders of magnitude higher than the pressure oscillations obtained in our calculations. A comparison is also performed with the wall pressure oscillations in a turbulent boundary layer for the same set of

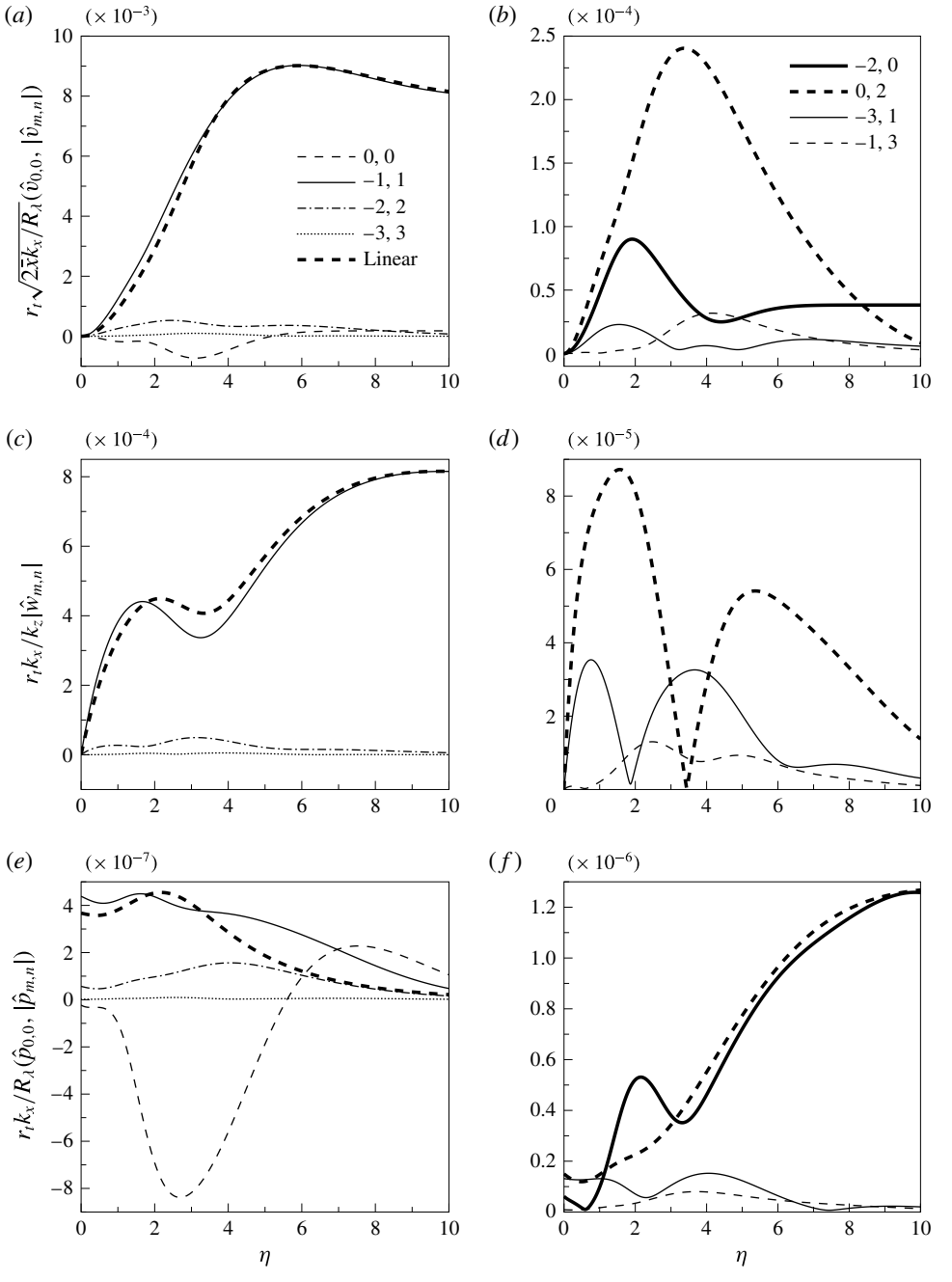

FIGURE 13. Profiles of the wall-normal velocity (*a*,*b*), spanwise velocity (*c*,*d*) and the pressure (*e*,*f*) of the mean-flow distortion and harmonics at $\bar{x} = 1.2$. The parameters correspond to the flight case with $M_\infty = 3$ and $r_t = 4.8$.

parameters. The experimental data provided by Tsuji *et al.* (2007), who measured the r.m.s. of the wall pressure at different friction Reynolds number R_τ, are used to evaluate the p_{rms} at the wall at the current friction Reynolds number $R_\tau = u_\tau^* x^*/\nu_\infty^*$,

where u_τ^* is the friction velocity and x^* is the distance from the leading edge. From our calculations we obtain $u_\tau^* = 13$ m s^{-1} and we choose $x^* = 0.7$ m corresponding to $\bar{x} = 1.2$. It follows that $R_\tau = 3.4 \times 10^4$. The relation proposed by Farabee & Casarella (1991) $(p_{rms}^+)^2 = 6.5 + 1.86 \ln(R_\tau/333)$ is employed to extrapolate the wall pressure r.m.s. p_{rms}^+ scaled with inner viscous units. The experiments of Tsuji *et al.* (2007) refer to an incompressible boundary layer and therefore the effect of the Mach number on the wall pressure needs to be included in our calculations. As a first estimate, the effect of compressibility on the skin-friction coefficient C_f is evaluated by means of figure 19.1 of Schlichting & Gersten (2000) and the same ratio $C_f(M_\infty = 3)/C_f(M_\infty = 0) = 0.6$ is assumed to be valid for the wall pressure. It follows that $p_{rms}^* = 35$ Pa and therefore the ratio between the wall pressure turbulent and pre-transitional fluctuations is approximately 6×10^2.

The total time-averaged ($m = 0$) streaks of the streamwise velocity and temperature, which will be referred to as u_{str} and τ_{str}, are defined as

$$\{u_{str}(\bar{x}, \eta, z), \tau_{str}(\bar{x}, \eta, z)\} = r_t \sum_{n=-\bar{N}_z}^{\bar{N}_z} \left\{\hat{u}_{0,n}, \hat{\tau}_{0,n}\right\} \mathrm{e}^{\mathrm{i}nk_z z}, \tag{5.6}$$

in which only modes with $n = 0, 2, 4, \ldots$ provide a non-zero contribution, but the component (0, 4) is almost negligible. They represent a time-averaged spanwise modulation superimposed onto the Blasius boundary layer.

Figure 14 shows the contours of the time-averaged streamwise velocity and the temperature streaks plotted in the η–z plane at different downstream locations. A positive value of the contours means that the mean flow is higher than the local Blasius solution, while a negative value means that it is lower. Therefore, near the wall the flow is accelerated and cooled, while close to the free stream it is decelerated and heated. The mean-flow distortion of the streamwise velocity has been interpreted as an increase of the mean wall shear stress and backward jets at the edge of the boundary layer, both of which have been observed in experiments (Ricco *et al.* 2011).

6. Summary and conclusions

The present work investigated the nonlinear response of a compressible boundary layer to free-stream unsteady vortical fluctuations of the convected-gust type. Attention is focused on the low-frequency and long streamwise components of the disturbances because these penetrate the most into the core of the boundary layer to form kinematic and thermal streaks (or Klebanoff modes). Thanks to this assumption, the mathematical framework of the compressible boundary-region equations (i.e. the Navier–Stokes equations with the streamwise derivative being neglected in the pressure and viscous terms) can be employed. The free-stream perturbation is assumed to be sufficiently strong that the amplitude of the induced streaks is comparable with the mean flow. Nonlinear effects must therefore be taken into account. The previous works by Ricco & Wu (2007) and Ricco *et al.* (2011) were extended to take into account both compressibility and nonlinear effects.

The boundary-layer displacement effect influences the outer-flow solution at leading order, that is, nonlinear interactions within the boundary layer generate a spanwise-independent flow, which drives an unsteady two-dimensional flow of acoustic nature in the outer inviscid region. The analysis shows that the displacement-induced part of the outer perturbation assumes different forms depending on the regime being subsonic or supersonic. Thanks to the well-known analogy with the flow over a thin

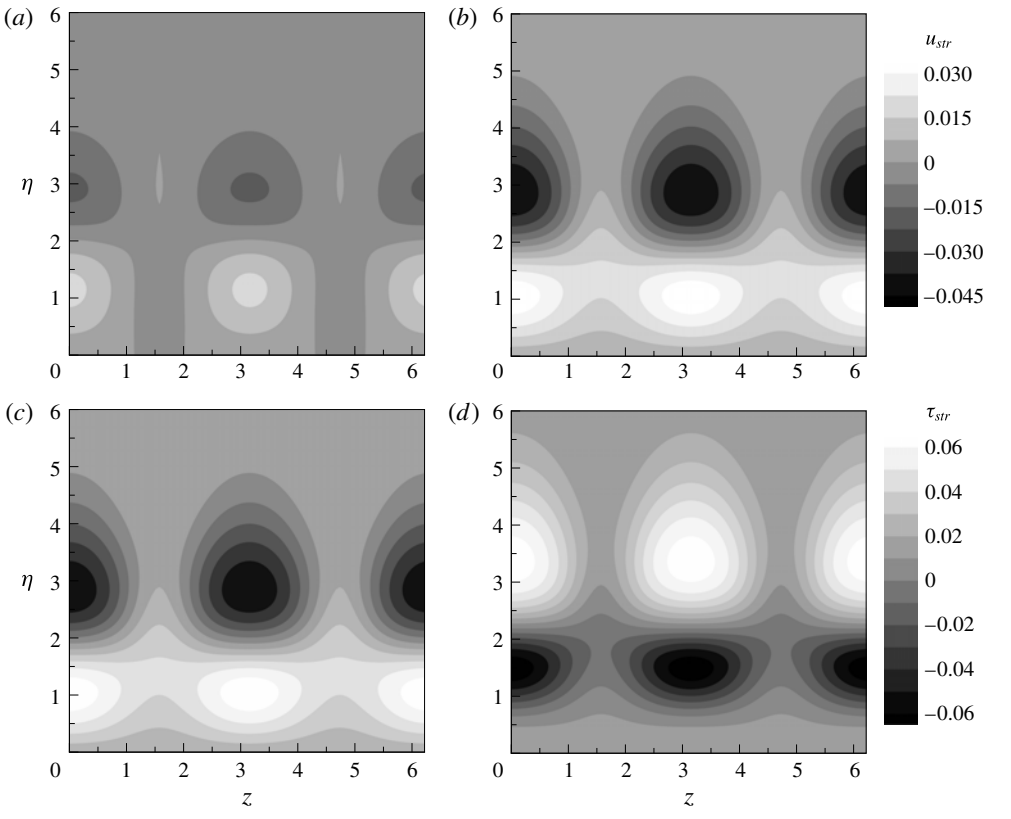

FIGURE 14. Contours of the time-averaged streamwise velocity streaks u_{str} (*a*,*b*) and the temperature streaks τ_{str} (*c*,*d*) in the η–z plane, at different downstream locations: $\bar{x} = 0.5$ (*a*,*c*), $\bar{x} = 1.2$ (*b*,*d*). The parameters correspond to the flight case with $M_\infty = 3$ and $r_t = 4.8$.

oscillating airfoil, analytical linearized solutions in the subsonic and supersonic cases are derived. This analogy is used here for the first time to study unsteady boundary layers. In the subsonic regime the disturbances propagate in all directions from the plate, while at supersonic speeds the fluid ahead of the body remains undisturbed and the perturbations are confined within the Mach dihedron.

An initial boundary-value problem, comprising the nonlinear unsteady compressible boundary-region equations and appropriate upstream and far-field conditions, is presented to study the formation and evolution of the streaks. The initial boundary-value problem is solved for the case where the convected gust consists of a pair of oblique modes with the same frequency but opposite spanwise wavenumbers. It is shown that nonlinear interactions inside the boundary layer generate higher harmonics and a mean-flow distortion. Kinematic and thermal streaks arise, which represent an unsteady spanwise modulation of the velocity and temperature superimposed onto the Blasius boundary layer. Nonlinearity attenuates the fluctuations of the streamwise velocity and a similar stabilizing effect on the temperature is identified. Near the wall the new mean streamwise velocity is higher than the local Blasius value, while the temperature profile exhibits a deficit with respect to the Blasius solution. At the edge of the boundary layer the flow is instead decelerated and heated. The effect

of the free-stream Mach number is also investigated: as the Mach number increases, the streamwise velocity fluctuations are inhibited, while the temperature ones are enhanced.

For the first time we have constructed the unsteady and three-dimensional base flow generated by the free-stream forcing and by the nonlinear interactions inside the boundary layer. This is the first step towards the formulation of the secondary instability problem, which, in the compressible case, must account for both the velocity and thermal streaks. Furthermore, by combining the present methodology and solutions, which pertain to very low-frequency disturbances, with the analytical results of Wu & Dong (2016) for components of $O(1)$ or higher frequency, it is now possible, for given broadband free-stream disturbances, to specify the appropriate inlet perturbations required by DNS of bypass transition in compressible boundary layers.

Acknowledgements

We would like to thank the Department of Mechanical Engineering at the University of Sheffield and the Institute of High Performance Computing in Singapore for funding this work. This research would have not been possible without the use of the high performance computing facilities of the A*Star Computational Resource Centre. P.R. is supported by UKTC EPSRC grant EP/L000261/1. Part of this material is based upon work carried out by P.R. and supported by the Air Force Office of Scientific Research under award number AFOSR Grant FA8655-13-1-3073. The authors are also grateful to Drs V.-T. Nguyen and M. Skote for helpful discussions and to Drs P. Hicks, D. Wise, W. Brevis, E. Klaseboer and Professor G. Vittori for insightful suggestions on a preliminary version of the manuscript. Part of this work was presented by E.M. at the 24th International Congress of Applied Mechanics in Montréal, Canada, in August 2016 and at the IUTAM-ABCM 8th Symposium on Laminar Turbulent Transition, Rio de Janeiro, Brazil, in September 2014.

Appendix A. Nonlinear terms of the boundary-region equations

The nonlinear terms $\hat{\mathcal{C}}_{m,n}$, $\hat{\mathcal{X}}_{m,n}$, $\hat{\mathcal{Y}}_{m,n}$, $\hat{\mathcal{Z}}_{m,n}$, $\hat{\mathcal{E}}_{m,n}$ of (2.23)–(2.27) are:

$$\hat{\mathcal{C}}_{m,n} = \left\{ -T\frac{\partial\widehat{\bar{\rho}\bar{u}}}{\partial\bar{x}} + \frac{\eta_c T}{2\bar{x}}\frac{\partial\widehat{\bar{\rho}\bar{u}}}{\partial\eta} - \frac{\partial\widehat{\bar{\rho}\bar{v}}}{\partial\eta} - \mathrm{i}nT\widehat{\bar{\rho}\bar{w}} + \mathrm{i}m\widehat{\bar{\rho}\bar{\tau}} + F'\frac{\partial\widehat{\bar{\rho}\bar{\tau}}}{\partial\bar{x}} - \frac{F}{2\bar{x}}\frac{\partial\widehat{\bar{\rho}\bar{\tau}}}{\partial\eta} \right\}_{m,n}, \quad (A\,1)$$

$$\begin{aligned}\hat{\mathcal{X}}_{m,n} = \Bigg\{ & \left(-\mathrm{i}mT + \frac{\eta_c T}{2\bar{x}}F'' + \frac{FT'}{2\bar{x}}\right)\widehat{\bar{\rho}\bar{u}} - F'T\frac{\partial\widehat{\bar{\rho}\bar{u}}}{\partial\bar{x}} + \frac{FT}{2\bar{x}}\frac{\partial\widehat{\bar{\rho}\bar{u}}}{\partial\eta} - \frac{\eta_c}{2\bar{x}}\frac{T'}{T}\widehat{\bar{u}\bar{u}} - \frac{\partial\widehat{\bar{u}\bar{u}}}{\partial\bar{x}} \\ & + \frac{\eta_c}{2\bar{x}}\frac{\partial\widehat{\bar{u}\bar{u}}}{\partial\eta} - r_t T\frac{\partial\widehat{\bar{\rho}\bar{u}\bar{u}}}{\partial\bar{x}} + r_t\frac{\eta_c T}{2\bar{x}}\frac{\partial\widehat{\bar{\rho}\bar{u}\bar{u}}}{\partial\eta} - F''\widehat{\bar{\rho}\bar{v}} + \frac{T'}{T^2}\widehat{\bar{u}\bar{v}} - \frac{1}{T}\frac{\partial\widehat{\bar{u}\bar{v}}}{\partial\eta} - r_t\frac{\partial\widehat{\bar{\rho}\bar{u}\bar{v}}}{\partial\eta} \\ & - \mathrm{i}n\widehat{\bar{u}\bar{w}} - r_t\mathrm{i}nT\widehat{\bar{\rho}\bar{u}\bar{w}} - \frac{FF''}{2\bar{x}}\widehat{\bar{\rho}\bar{\tau}} + \frac{1}{2\bar{x}}\left(\frac{\mu'}{T}\right)'\widehat{\bar{\tau}\frac{\partial\bar{u}}{\partial\eta}} + \frac{\mu'}{2\bar{x}T}\frac{\partial}{\partial\eta}\left(\widehat{\bar{\tau}\frac{\partial\bar{u}}{\partial\eta}}\right) \\ & + \mathrm{i}n\kappa^2 T\mu'\widehat{\bar{\tau}\frac{\partial\bar{u}}{\partial\hat{z}}} + \frac{1}{2\bar{x}}\left(\frac{F''}{T}\right)'\hat{\mu} + \frac{F''}{2\bar{x}T}\frac{\partial\hat{\mu}}{\partial\eta} - \frac{r_t T'}{2\bar{x}T^2}\widehat{\bar{\mu}\frac{\partial\bar{u}}{\partial\eta}} + \frac{r_t}{2\bar{x}T}\frac{\partial}{\partial\eta}\left(\widehat{\bar{\mu}\frac{\partial\bar{u}}{\partial\eta}}\right) \\ & + r_t\mathrm{i}nT\kappa^2\widehat{\bar{\mu}\frac{\partial\bar{u}}{\partial\hat{z}}} \Bigg\}_{m,n}, \end{aligned} \quad (A\,2)$$

$$\hat{\mathcal{Y}}_{m,n} = \Bigg\{ -\frac{T}{4\bar{x}^2}\left[FT + \eta_c(FT' - TF') - \eta_c^2 F''T\right]\widehat{\bar{\rho}\bar{u}}$$
$$- \left(\mathrm{i}mT + \frac{\eta_c TF'' + F'T}{2\bar{x}} - \frac{FT'}{\bar{x}}\right)\widehat{\bar{\rho}\bar{v}}$$
$$- F'T\frac{\partial\widehat{\bar{\rho}\bar{v}}}{\partial\bar{x}} + \frac{FT}{2\bar{x}}\frac{\partial\widehat{\bar{\rho}\bar{v}}}{\partial\eta} - \frac{1}{2\bar{x}}\left(1 + \frac{\eta_c T'}{T}\right)\widehat{\bar{u}\bar{v}} - \frac{\partial\widehat{\bar{u}\bar{v}}}{\partial\bar{x}} + \frac{\eta_c}{2\bar{x}}\frac{\partial\widehat{\bar{u}\bar{v}}}{\partial\bar{\eta}} - r_t\frac{T}{2\bar{x}}\widehat{\bar{\rho}\bar{u}\bar{v}}$$
$$- r_t T\frac{\partial\widehat{\bar{\rho}\bar{u}\bar{v}}}{\partial\bar{x}} + r_t\frac{\eta_c T}{2\bar{x}}\frac{\partial\widehat{\bar{\rho}\bar{u}\bar{v}}}{\partial\eta} + \frac{T'}{T^2}\widehat{\bar{v}\bar{v}} - \frac{1}{T}\frac{\partial\widehat{\bar{v}\bar{v}}}{\partial\eta} - r_t\frac{\partial\widehat{\bar{\rho}\bar{v}\bar{v}}}{\partial\eta} - \mathrm{i}n\widehat{\bar{v}\bar{w}} - r_t\mathrm{i}nT\widehat{\bar{\rho}\bar{v}\bar{w}}$$
$$+ \frac{T}{4\bar{x}^2}\left[-\eta_c(FF')' + FF' + \frac{F^2T'}{T}\right]\widehat{\bar{\rho}\bar{\tau}} - \frac{\mu''T'}{3\bar{x}}\widehat{\bar{\tau}\frac{\partial\bar{u}}{\partial\bar{x}}} - \frac{\mu'}{3\bar{x}}\frac{\partial}{\partial\eta}\left(\widehat{\bar{\tau}\frac{\partial\bar{u}}{\partial\bar{x}}}\right)$$
$$- \frac{1}{12\bar{x}^2}\left[\mu' + \eta_c T\left(\frac{\mu'}{T}\right)'\right]\widehat{\bar{\tau}\frac{\partial\bar{u}}{\partial\eta}} + \frac{\mu'}{2\bar{x}}\frac{\partial}{\partial\bar{x}}\left(\widehat{\bar{\tau}\frac{\partial\bar{u}}{\partial\eta}}\right) - \frac{\eta_c\mu'}{12\bar{x}^2}\frac{\partial}{\partial\eta}\left(\widehat{\bar{\tau}\frac{\partial\bar{u}}{\partial\eta}}\right)$$
$$+ \frac{2}{3\bar{x}}\left(\frac{\mu'}{T}\right)'\widehat{\bar{\tau}\frac{\partial\bar{v}}{\partial\eta}} + \frac{2\mu'}{3\bar{x}T}\frac{\partial}{\partial\eta}\left(\widehat{\bar{\tau}\frac{\partial\bar{v}}{\partial\eta}}\right) + \mathrm{i}n\kappa^2 T\mu'\widehat{\bar{\tau}\frac{\partial\bar{v}}{\partial\hat{z}}} + \frac{\mathrm{i}n\mu'}{2\bar{x}}\widehat{\bar{\tau}\frac{\partial\bar{w}}{\partial\eta}} - \frac{\mu''T'}{3\bar{x}}\widehat{\bar{\tau}\frac{\partial\bar{w}}{\partial\hat{z}}}$$
$$- \frac{\mu'}{3\bar{x}}\frac{\partial}{\partial\eta}\left(\widehat{\bar{\tau}\frac{\partial\bar{w}}{\partial\hat{z}}}\right) + \left[\frac{F(T')^2}{3\bar{x}^2T^2} + \frac{F''}{4\bar{x}^2} - \frac{\eta_c T'F''}{4\bar{x}^2T} - \frac{(FT')'}{3\bar{x}^2T} + \frac{\eta_c F''''}{4\bar{x}^2}\right]\hat{\mu}$$
$$+ \frac{F''}{2\bar{x}}\frac{\partial\hat{\mu}}{\partial\bar{x}} + \left(\frac{\eta_c F''}{4\bar{x}^2} - \frac{FT'}{3\bar{x}^2T}\right)\frac{\partial\hat{\mu}}{\partial\eta} - \frac{r_t}{3\bar{x}}\frac{\partial}{\partial\eta}\left(\widehat{\bar{\mu}\frac{\partial\bar{u}}{\partial\bar{x}}}\right) + \frac{r_t}{12\bar{x}^2}\left(\frac{\eta_c T'}{T} - 1\right)\widehat{\bar{\mu}\frac{\partial\bar{u}}{\partial\eta}}$$
$$+ \frac{r_t}{2\bar{x}}\frac{\partial}{\partial\bar{x}}\left(\widehat{\bar{\mu}\frac{\partial\bar{u}}{\partial\eta}}\right) - \frac{r_t\eta_c}{12\bar{x}^2}\frac{\partial}{\partial\eta}\left(\widehat{\bar{\mu}\frac{\partial\bar{u}}{\partial\eta}}\right) - r_t\frac{2T'}{3\bar{x}T^2}\widehat{\bar{\mu}\frac{\partial\bar{v}}{\partial\eta}} + \frac{2r_t}{3\bar{x}T}\frac{\partial}{\partial\eta}\left(\widehat{\bar{\mu}\frac{\partial\bar{v}}{\partial\eta}}\right)$$
$$+ r_t\mathrm{i}nT\kappa^2\widehat{\bar{\mu}\frac{\partial\bar{v}}{\partial\hat{z}}} + r_t\frac{\mathrm{i}n}{2\bar{x}}\widehat{\bar{\mu}\frac{\partial\bar{w}}{\partial\eta}} - \frac{r_t}{3\bar{x}}\frac{\partial}{\partial\eta}\left(\widehat{\bar{\mu}\frac{\partial\bar{w}}{\partial\hat{z}}}\right)\Bigg\}_{m,n}, \tag{A 3}$$

$$\hat{\mathcal{Z}}_{m,n} = \Bigg\{ \left(-\mathrm{i}mT + \frac{FT'}{2\bar{x}}\right)\widehat{\bar{\rho}\bar{w}} - F'T\frac{\partial\widehat{\bar{\rho}\bar{w}}}{\partial\bar{x}} + \frac{FT}{2\bar{x}}\frac{\partial\widehat{\bar{\rho}\bar{w}}}{\partial\eta} - \frac{\eta_c T'}{2\bar{x}T}\widehat{\bar{u}\bar{w}} - \frac{\partial\widehat{\bar{u}\bar{w}}}{\partial\bar{x}} + \frac{\eta_c}{2\bar{x}}\frac{\partial\widehat{\bar{u}\bar{w}}}{\partial\eta}$$
$$- r_t T\frac{\partial\widehat{\bar{\rho}\bar{u}\bar{w}}}{\partial\bar{x}} + r_t\frac{\eta_c T}{2\bar{x}}\frac{\partial\widehat{\bar{\rho}\bar{u}\bar{w}}}{\partial\eta} + \frac{T'}{T^2}\widehat{\bar{v}\bar{w}} - \frac{1}{T}\frac{\partial\widehat{\bar{v}\bar{w}}}{\partial\eta} - r_t\frac{\partial\widehat{\bar{\rho}\bar{v}\bar{w}}}{\partial\eta} - \mathrm{i}n\widehat{\bar{w}\bar{w}} - r_t\mathrm{i}nT\widehat{\bar{\rho}\bar{w}\bar{w}}$$
$$- \frac{2\mathrm{i}nT\kappa^2\mu'}{3}\widehat{\bar{\tau}\frac{\partial\bar{u}}{\partial\bar{x}}} + \frac{\mathrm{i}nT\kappa^2\mu'\eta_c}{3\bar{x}}\widehat{\bar{\tau}\frac{\partial\bar{u}}{\partial\eta}} - \frac{\eta_c\kappa^2\mu''TT'}{2\bar{x}}\widehat{\bar{\tau}\frac{\partial\bar{u}}{\partial\hat{z}}} + T\mu'\kappa^2\frac{\partial}{\partial\bar{x}}\left(\widehat{\bar{\tau}\frac{\partial\bar{u}}{\partial\hat{z}}}\right)$$
$$- \frac{\eta_c\kappa^2 T\mu'}{2\bar{x}}\frac{\partial}{\partial\eta}\left(\widehat{\bar{\tau}\frac{\partial\bar{u}}{\partial\hat{z}}}\right) - \frac{2\mathrm{i}n\kappa^2\mu'}{3}\widehat{\bar{\tau}\frac{\partial\bar{v}}{\partial\eta}} + \mu''T'\kappa^2\widehat{\bar{\tau}\frac{\partial\bar{v}}{\partial\hat{z}}} + \mu'\kappa^2\frac{\partial}{\partial\eta}\left(\widehat{\bar{\tau}\frac{\partial\bar{v}}{\partial\hat{z}}}\right)$$
$$+ \frac{1}{2\bar{x}}\left(\frac{\mu'}{T}\right)'\widehat{\bar{\tau}\frac{\partial\bar{w}}{\partial\eta}} + \frac{\mu'}{2\bar{x}T}\frac{\partial}{\partial\eta}\left(\widehat{\bar{\tau}\frac{\partial\bar{w}}{\partial\eta}}\right) + \frac{4\mu'\mathrm{i}nT\kappa^2}{3}\widehat{\bar{\tau}\frac{\partial\bar{w}}{\partial\hat{z}}} + \frac{\mathrm{i}n\kappa^2FT'}{3\bar{x}}\hat{\mu}$$
$$- r_t\frac{2\mathrm{i}nT\kappa^2}{3}\widehat{\bar{\mu}\frac{\partial\bar{u}}{\partial\bar{x}}} + r_t\frac{\mathrm{i}nT\kappa^2\eta_c}{3\bar{x}}\widehat{\bar{\mu}\frac{\partial\bar{u}}{\partial\eta}} + r_t T\kappa^2\frac{\partial}{\partial\bar{x}}\left(\widehat{\bar{\mu}\frac{\partial\bar{u}}{\partial\hat{z}}}\right) - r_t\frac{\eta_c T\kappa^2}{2\bar{x}}\frac{\partial}{\partial\eta}\left(\widehat{\bar{\mu}\frac{\partial\bar{u}}{\partial\hat{z}}}\right)$$

$$
\begin{aligned}
&- r_t \frac{2\mathrm{i}n\kappa^2}{3}\widehat{\bar{\mu}\frac{\partial \bar{v}}{\partial \eta}} + r_t\kappa^2\frac{\partial}{\partial \eta}\left(\widehat{\bar{\mu}\frac{\partial \bar{v}}{\partial \hat{z}}}\right) - r_t\frac{T'}{2\bar{x}T^2}\widehat{\mu\frac{\partial \bar{w}}{\partial \eta}} + \frac{r_t}{2\bar{x}T}\frac{\partial}{\partial \eta}\left(\widehat{\bar{\mu}\frac{\partial \bar{w}}{\partial \eta}}\right)\\
&+ r_t\frac{4\mathrm{i}nT\kappa^2}{3}\widehat{\bar{\mu}\frac{\partial \bar{w}}{\partial \hat{z}}}\Bigg\}_{m,n}, \qquad \text{(A 4)}\\
\hat{\mathcal{E}}_{m,n} = &\Bigg\{\frac{\eta_c T'T}{2\bar{x}}\widehat{\bar{\rho}\bar{u}} - r_t T\frac{\partial\widehat{\bar{\rho}\bar{u}\bar{\tau}}}{\partial \bar{x}} + r_t\frac{\eta_c T}{2\bar{x}}\frac{\partial\widehat{\bar{\rho}\bar{u}\bar{\tau}}}{\partial \eta} - T'\widehat{\bar{\rho}\bar{v}} - r_t\frac{\partial\widehat{\bar{\rho}\bar{v}\bar{\tau}}}{\partial \eta} - r_t\mathrm{i}nT\widehat{\bar{\rho}\bar{w}\bar{\tau}} - \mathrm{i}mT\widehat{\bar{\rho}\bar{\tau}}\\
&- F'T\frac{\partial\widehat{\bar{\rho}\bar{\tau}}}{\partial \bar{x}} + \frac{FT}{2\bar{x}}\frac{\partial\widehat{\bar{\rho}\bar{\tau}}}{\partial \eta} - \frac{\eta_c T'}{2\bar{x}T}\widehat{\bar{u}\bar{\tau}} - \frac{\partial\widehat{\bar{u}\bar{\tau}}}{\partial \bar{x}} + \frac{\eta_c}{2\bar{x}}\frac{\partial\widehat{\bar{u}\bar{\tau}}}{\partial \eta} + \frac{T'}{T^2}\widehat{\bar{v}\bar{\tau}} - \frac{1}{T}\frac{\partial\widehat{\bar{v}\bar{\tau}}}{\partial \eta} - \mathrm{i}n\widehat{\bar{w}\bar{\tau}}\\
&- \frac{\mu' Tn^2\kappa^2}{2Pr}\widehat{\bar{\tau}^2} + \frac{1}{2\bar{x}Pr}\left(\frac{\mu'}{T}\right)'\widehat{\bar{\tau}\frac{\partial \bar{\tau}}{\partial \eta}} + \frac{\mu'}{2\bar{x}PrT}\frac{\partial}{\partial \eta}\left(\widehat{\bar{\tau}\frac{\partial \bar{\tau}}{\partial \eta}}\right)\\
&+ \frac{M_\infty^2(\gamma-1)\mu}{2\bar{x}T}\widehat{\left(\frac{\partial \bar{u}}{\partial \eta}\right)^2} + \frac{M_\infty^2(\gamma-1)\mu' F''}{\bar{x}T}\widehat{\frac{\partial \bar{u}}{\partial \eta}\bar{\tau}} + r_t\frac{M_\infty^2(\gamma-1)\mu'}{2\bar{x}T}\widehat{\left(\frac{\partial \bar{u}}{\partial \eta}\right)^2\bar{\tau}}\\
&+ M_\infty^2(\gamma-1)\kappa^2 T\mu\widehat{\left(\frac{\partial \bar{u}}{\partial \hat{z}}\right)^2} + M_\infty^2(\gamma-1)r_t\kappa^2 T\mu'\widehat{\left(\frac{\partial \bar{u}}{\partial \hat{z}}\right)^2\bar{\tau}}\\
&+ \left[\frac{1}{2\bar{x}Pr}\left(\frac{T'}{T}\right)' + \frac{M_\infty^2(\gamma-1)(F'')^2}{2\bar{x}T}\right]\hat{\mu} + \frac{T'}{2\bar{x}PrT}\frac{\partial \hat{\mu}}{\partial \eta}\\
&+ r_t\frac{M_\infty^2(\gamma-1)F''}{\bar{x}T}\widehat{\bar{\mu}\frac{\partial \bar{u}}{\partial \eta}} + r_t^2\frac{M_\infty^2(\gamma-1)}{2\bar{x}T}\widehat{\bar{\mu}\left(\frac{\partial \bar{u}}{\partial \eta}\right)^2} + r_t^2 M_\infty^2(\gamma-1)T\kappa^2\widehat{\bar{\mu}\left(\frac{\partial \bar{u}}{\partial \hat{z}}\right)^2}\\
&- r_t\frac{T'}{2\bar{x}PrT^2}\widehat{\bar{\mu}\frac{\partial \bar{\tau}}{\partial \eta}} + \frac{r_t}{2\bar{x}PrT}\frac{\partial}{\partial \eta}\left(\widehat{\bar{\mu}\frac{\partial \bar{\tau}}{\partial \eta}}\right) + r_t\frac{\mathrm{i}nT\kappa^2}{Pr}\widehat{\bar{\mu}\frac{\partial \bar{\tau}}{\partial \hat{z}}}\Bigg\}_{m,n}, \qquad \text{(A 5)}
\end{aligned}
$$

where $\hat{z} = k_z z$.

REFERENCES

ABRAMOWITZ, M. & STEGUN, I. A. 1964 *Handbook of Mathematical Functions: Applied Mathematics Series, No. 55*. National Bureau of Standards.

ANDERSON, J. D. JR. 2006 *Hypersonic and High-Temperature Gas Dynamics*, 2nd edn. AIAA.

ANDERSON, J. D. JR. 2007 *Fundamentals of Aerodynamics*, 4th edn. McGraw-Hill.

ANDERSSON, P., BERGGREN, M. & HENNINGSON, D. S. 1999 Optimal disturbances and bypass transition in boundary layers. *Phys. Fluids* **11** (1), 134–150.

ARNAL, D. & JUILLEN, J. C. 1978 Contribution expérimentale à l'étude de la reptivité d'une couche limite laminaire à la turbulence de l'écoulement général. *CERT RT 1/5018 AYD – ONERA*.

BECKWITH, I. E. & MILLER, C. G. III 1990 Aerothermodynamics and transition in high-speed wind tunnels at NASA Langley. *Annu. Rev. Fluid Mech.* **22** (1), 419–439.

BRANDT, L., SCHLATTER, P. & HENNINGSON, D. S. 2004 Transition in boundary layers subject to free-stream turbulence. *J. Fluid Mech.* **517**, 167–198.

BRINKERHOFF, J. R. & YARAS, M. I. 2015 Numerical investigation of transition in a boundary layer subjected to favourable and adverse streamwise pressure gradients and elevated free stream turbulence. *J. Fluid Mech.* **781**, 52–86.

CAMCI, C. & ARTS, T. 1990 An experimental convective heat transfer investigation around a film-cooled gas turbine blade. *Trans. ASME J. Turbomach.* **112** (3), 497–503.

CANUTO, C., HUSSAINI, M. Y., QUARTERONI, A. & ZANG, T. A. 1988 *Spectral Methods in Fluid Dynamics*. Springer.

CHAMPION, K. S. W., COLE, A. E. & KANTOR, A. J. 1985 Standard and reference atmospheres. In *Handbook of Geophysics and the Space Environment*, vol. 14. Air Force Geophysics Laboratory.

CHANG, C.-L., MALIK, M. R., ERLEBACHER, M. Y. & HUSSAINI, M. Y. 1991 Compressible stability of growing boundary layers using parabolized stability equations. *AIAA Paper* 91-1636.

CHANG, C.-L., MALIK, M. R. & HUSSAINI, M. Y. 1990 Effects of shock on the stability of hypersonic boundary layers. *AIAA Paper* 90-1448.

COLEMAN, T. L. & STEINER, R. 1960 Atmospheric turbulence measurements obtained from airplane operations at altitudes between 20 000 and 75 000 feet for several areas in the northern hemisphere. *NASA Tech. Rep.* NASA/TN D-548.

COWLEY, S. J. & HALL, P. 1990 On the instability of hypersonic flow past a wedge. *J. Fluid Mech.* **214**, 17–42.

DONG, M. & WU, X. 2013 On continuous spectra of the Orr–Sommerfeld/Squire equations and entrainment of free-stream vortical disturbances. *J. Fluid Mech.* **732**, 616–659.

DONGARRA, J., LUMSDAINE, A., POZO, R. & REMINGTON, K. 2006 IML++ v. 1.2 Iterative Method Library. http://math.nist.gov/iml++/.

DOWELL, E. H. 2014 *A Modern Course in Aeroelasticity*, vol. 217. Springer.

DRAGOS, L. 2004 *Mathematical Methods in Aerodynamics*. Springer.

EHERNBERGER, L. J. & LOVE, B. J. 1975 High altitude gust acceleration environment as experienced by a supersonic airplane. *NASA Tech. Rep.* NASA/TN D-7868.

FARABEE, T. M. & CASARELLA, M. J. 1991 Spectral features of wall pressure fluctuations beneath turbulent boundary layers. *Phys. Fluids* **3**, 2410–2420.

FEDOROV, A. V. & KHOKHLOV, A. P. 2001 Prehistory of instability in a hypersonic boundary layer. *Theor. Comput. Fluid Dyn.* **14**, 359–375.

FEDOROV, A. V. & KHOKHLOV, A. P. 2003 Receptivity of a high-speed boundary layer to acoustic disturbances. *J. Fluid Mech.* **491**, 101–129.

FEDOROV, A., SHIPLYUK, A., MASLOV, A., BUROV, E. & MALMUTH, N. 2003 Stabilization of a hypersonic boundary layer using an ultrasonically absorptive coating. *J. Fluid Mech.* **479**, 99–124.

FRANSSON, J. H. M., MATSUBARA, M. & ALFREDSSON, P. H. 2005 Transition induced by free-stream turbulence. *J. Fluid Mech.* **527**, 1–25.

GOLDSTEIN, M. E. 1997 Response of the pre-transitional laminar boundary layer to free-stream turbulence – Otto Laporte Lecture. *Bull. Am. Phys. Soc.* **42**, 2150.

GOLDSTEIN, M. E. & LEIB, S. J. 1993 Three-dimensional boundary layer instability and separation induced by small-amplitude streamwise vorticity in the upstream flow. *J. Fluid Mech.* **246**, 21–41.

GOLDSTEIN, M. E., LEIB, S. J. & COWLEY, S. J. 1992 Distortion of a flat plate boundary layer by free stream vorticity normal to the plate. *J. Fluid Mech.* **237**, 231–260.

GRAZIOSI, P. & BROWN, G. L. 2002 Experiments on stability and transition at Mach 3. *J. Fluid Mech.* **472**, 83–124.

HOCKING, W. K. 1985 Measurement of turbulent energy dissipation rates in the middle atmosphere by radar techniques: a review. *Radio Sci.* **20** (6), 1403–1422.

JACOBS, R. G. & DURBIN, P. A. 2001 Simulation of bypass transition. *J. Fluid Mech.* **428**, 185–212.

JOO, J. & DURBIN, P. 2012 Continuous mode transition in high-speed boundary-layers. *Flow Turbul. Combust.* **88**, 407–430.

KEMP, N. 1951 The laminar three-dimensional boundary layer and a study of the flow past a side edge. MSc thesis, Cornell University.

KENDALL, J. M. 1967 Supersonic boundary layer stability experiments. *Tech. Rep.* Air Force Report BSD-TR-67-213, vol. II.

KENDALL, J. M. 1975 Wind tunnel experiments relating to supersonic and hypersonic boundary-layer transition. *AIAA J.* **13** (3), 290–299.

KENDALL, J. M. 1985 Experimental study of disturbances produced in a pre-transitional laminar boundary layer by weak freestream turbulence. *AIAA Paper* 85-1695.

KENDALL, J. M. 1990 Boundary layer receptivity to free stream turbulence. *AIAA Paper* 90-1504.

KENDALL, J. M. 1991 Studies on laminar boundary layer receptivity to free-stream turbulence near a leading edge. In *Boundary Layer Stability and Transition to Turbulence* (ed. D. C. Reda, H. L. Reed & R. Kobayashi), vol. 114, pp. 23–30. ASME FED.

KLEBANOFF, P. S. 1971 Effect of free-stream turbulence on a laminar boundary layer. *Bull. Am. Phys. Soc.* **16**, 1323.

LANDAHL, M. T. 1989 *Unsteady Transonic Flow*. Cambridge University Press.

LAUFER, J. 1961 Aerodynamic noise in supersonic wind tunnels. *J. Aero. Sci.* **28** (9), 685–692.

LEES, L. 1947 The stability of the laminar boundary layer in a compressible fluid. *NACA TN* 876.

LEIB, S. J., WUNDROW, D. W. & GOLDSTEIN, M. E. 1999 Effect of free-stream turbulence and other vortical disturbances on a laminar boundary layer. *J. Fluid Mech.* **380**, 169–203.

LI, F. & MALIK, M. R. 1996 On the nature of PSE approximation. *Theor. Comput. Fluid Dyn.* **8** (4), 253–273.

LIGHTHILL, M. J. 1958 On displacement thickness. *J. Fluid Mech.* **4** (04), 383–392.

MACK, L. M. 1975 Linear stability theory and the problem of supersonic boundary-layer transition. *AIAA J.* **13** (3), 278–289.

MACK, L. M. 1984 Boundary-layer linear stability theory. *Special Course on Stability and Transition of Laminar flow, AGARD Report* 709, pp. 1–81. Jet Propulsion Laboratory, California Institute of Technology, Pasadena.

MATSUBARA, M. & ALFREDSSON, P. H. 2001 Disturbance growth in boundary layers subjected to free-stream turbulence. *J. Fluid Mech.* **430**, 149–168.

MAYER, C. S. J., VON TERZI, D. A. & FASEL, H. F. 2011 Direct numerical simulation of complete transition to turbulence via oblique breakdown at Mach 3. *J. Fluid Mech.* **674**, 5–42.

MCKENZIE, J. F. & WESTPHAL, K. O. 1968 Interaction of linear waves with oblique shock waves. *Phys. Fluids* **11** (11), 2350–2362.

MORKOVIN, M. V. 1984 Bypass transition to turbulence and research desiderata. In *NASA CP-2386 Transition in Turbines*, pp. 161–204. NASA.

NAGARAJAN, S., LELE, S. K. & FERZIGER, J. H. 2007 Leading-edge effects in bypass transition. *J. Fluid Mech.* **572**, 471–504.

OVCHINNIKOV, V., CHOUDHARI, M. M. & PIOMELLI, U. 2008 Numerical simulations of boundary-layer bypass transition due to high-amplitude free-stream turbulence. *J. Fluid Mech.* **613**, 135–169.

PATE, S. R. & SCHUELER, C. J. 1969 Radiated aerodynamic noise effects on boundary-layer transition in supersonic and hypersonic wind tunnels. *AIAA J.* **7** (3), 450–457.

QIN, F. & WU, X. 2016 Response and receptivity of the hypersonic boundary layer past a wedge to free-stream acoustic, vortical and entropy disturbances. *J. Fluid Mech.* **797**, 874–915.

RICCO, P. 2006 Response of a compressible laminar boundary layer to free-stream turbulence. PhD thesis, University of London.

RICCO, P., LUO, J. & WU, X. 2011 Evolution and instability of unsteady nonlinear streaks generated by free-stream vortical disturbances. *J. Fluid Mech.* **677**, 1–38.

RICCO, P., SHAH, D. & HICKS, P. D. 2013 Compressible laminar streaks with wall suction. *Phys. Fluids* **25**, 054110.

RICCO, P., TRAN, D.-L. & YE, G. 2009 Wall heat transfer effects on Klebanoff modes and Tollmien-Schlichting waves in a compressible boundary layer. *Phys. Fluids* **21**, 024106.

RICCO, P. & WU, X. 2007 Response of a compressible laminar boundary layer to free-stream vortical disturbances. *J. Fluid Mech.* **587**, 97–138.

RIEDEL, H. & SITZMANN, M. 1998 In-flight investigations of atmospheric turbulence. *Aerosp. Sci. Technol.* **2** (5), 301–319.

SAAD, Y. & SCHULTZ, M. H. 1986 GMRES: a generalized minimal residual algorithm for solving nonsymmetric linear systems. *SIAM J. Sci. Stat. Comput.* **7** (3), 856–869.

SARIC, W. S. 2008 Flight experiments on local and global effects of surface roughness on 2-d and 3-d boundary-layer stability and transition. *Tech. Rep.* DTIC Document.

SCHLICHTING, H. & GERSTEN, K. 2000 *Boundary-Layer Theory*. Springer.

SCHNEIDER, S. P. 1999 Flight data for boundary-layer transition at hypersonic and supersonic speeds. *J. Spacecr. Rockets* **36** (1), 8–20.

SCHNEIDER, S. P. 2001 Effect of high-speed tunnel noise on laminar-turbulent transition. *J. Spacecr Rockets* **38** (3), 323–333.

STEWARTSON, K. 1950 On the linearized potential theory of unsteady supersonic motion. *Q. J. Mech. Appl. Maths* **3** (2), 182–199.

STEWARTSON, K. 1964 *The Theory of Laminar Boundary Layers in Compressible Fluids*. Clarendon Press.

TAYLOR, G. I. 1939 Some recent developments in the study of turbulence. In *Proceedings of the Fifth International Congress for Applied Mechanics* (ed. J. P. Den Hartog & H. Peters), pp. 294–310. Wiley/Chapman and Hall.

TSUJI, Y., FRANSSON, J. H. M., ALFREDSSON, P. H. & JOHANSSON, A. V. 2007 Pressure statistics and their scaling in high-Reynolds-number turbulent boundary layers. *J. Fluid Mech.* **585**, 1–40.

VAN DYKE, M. 1975 *Perturbation Methods in Fluid Mechanics*. Parabolic.

WESTIN, K. J. A., BAKCHINOV, A. A., KOZLOV, V. V. & ALFREDSSON, P. H. 1998 Experiments on localized disturbances in a flat plate boundary layer. Part 1. The receptivity and the evolution of a localized free-stream disturbance. *Eur. J. Mech. (*B*/Fluids)* **17**, 823–846.

WESTIN, K. J. A., BOIKO, A. V., KLINGMANN, B. G. B., KOZLOV, V. V. & ALFREDSSON, P. H. 1994 Experiments in a boundary layer subjected to free stream turbulence. Part 1. Boundary layer structure and receptivity. *J. Fluid Mech.* **281**, 193–218.

WILSON, R. J., LOVE, B. J. & LARSON, R. R. 1971 Evaluation of effects of high-altitude turbulence encounters on the XB-70 airplane. *NASA Tech. Rep.* NASA/TN D-6457.

WU, X. & CHOUDHARI, M. 2003 Linear and non-linear instabilities of a Blasius boundary layer perturbed by streamwise vortices. Part 2. Intermittent instability induced by long-wavelength Klebanoff modes. *J. Fluid Mech.* **483**, 249–286.

WU, X. & DONG, M. 2016 Entrainment of short-wavelength free-stream vortical disturbances in compressible and incompressible boundary layers. *J. Fluid Mech.* **797**, 683–728.

WU, X. & LUO, J. 2003 Linear and non-linear instabilities of a Blasius boundary layer perturbed by streamwise vortices. Part 1. Steady streaks. *J. Fluid Mech.* **483**, 225–248.

WU, X., ZHAO, D. & LUO, J. 2011 Excitation of steady and unsteady gortler vortices by free-stream vortical disturbances. *J. Fluid Mech.* **682**, 66–100.

WUNDROW, D. W. & GOLDSTEIN, M. E. 2001 Effect on a laminar boundary layer of small-amplitude streamwise vorticity in the upstream flow. *J. Fluid Mech.* **426**, 229–262.

ZAKI, T. & DURBIN, P. A. 2005 Mode interaction and the bypass route to transition. *J. Fluid Mech.* **531**, 85–111.

ZANIN, B. Y. 1985 Transition at natural conditions and comparison with the results of wind tunnel studies. In *Laminar-Turbulent Transition*, pp. 541–546. Springer.

ZHANG, Q. & HE, L. 2014 Impact of wall temperature on turbine blade tip aerothermal performance. *Trans. ASME J. Engng Gas Turbines Power* **136** (5), 052602.

ZHANG, Y., ZAKI, T., SHERWIN, S. & WU, X. 2011 Nonlinear response of a laminar boundary layer to isotropic and spanwise localized free-stream turbulence. In *The 6th AIAA Theoretical Fluid Mechanics Conference*, p. 3292. American Institute of Aeronautics and Astronautics.

ZHONG, X. & WANG, X. 2012 Direct numerical simulation on the receptivity, instability, and transition of hypersonic boundary layers. *Annu. Rev. Fluid Mech.* **44**, 527–561.

ZUCCHER, S., BOTTARO, A. & LUCHINI, P. 2006 Algebraic growth in a Blasius boundary layer: nonlinear optimal disturbances. *Eur. J. Mech. (*B*/Fluids)* **25** (1), 1–17.